NASA Technical Memorandum 110174

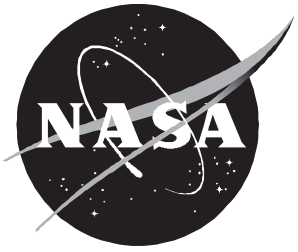

Solution of the Three-Dimensional Helmholtz Equation with Nonlocal Boundary Conditions

Steve L. Hodge
Virginia Consortium for Engineering and Science, Hampton, Virginia

William E. Zorumski and Willie R. Watson
Langley Research Center, Hampton, Virginia

May 1995

National Aeronautics and
Space Administration
Langley Research Center
Hampton, Virginia 23681-0001

Abstract

The Helmholtz equation is solved within a three-dimensional rectangular duct with a sound source at the duct entrance plane, local admittance conditions on the side walls, and a new, nonlocal *radiation* boundary condition at the duct exit plane. The formulation employs a truncation of an infinite matrix, the *generalized modal admittance tensor*, that represents the transformation of the modal pressure coefficients to the modal axial velocity coefficients. This condition accurately models the acoustic admittance (a relationship between the velocity and pressure of an acoustic wave) at an arbitrary computational boundary plane. In particular, the proper physical admittance may correspond to a *nonreflecting* radiation condition on an arbitrarily located boundary plane that is used to limit the size of the computational domain. A linear system of equations is constructed with second-order central differences for the Helmholtz operator and second-order backward differences for both local admittance conditions and the gradient term in the nonlocal radiation boundary condition. The resulting matrix equation is large, sparse, and non-Hermitian. The size and structure of the matrix makes direct solution techniques impractical; as a result, a nonstationary iterative technique is used for its solution. The theory behind the nonstationary technique is reviewed, and numerical results are presented for radiation from both a point source and a planar acoustic source in both soft-walled and hard-walled ducts. The solutions with the nonlocal boundary conditions are invariant to the location of the computational boundary, and the same nonlocal conditions are valid for all solutions. The nonlocal conditions thus provide a means of minimizing the size of three-dimensional computational domains.

1 Introduction

Computational aeroacoustics requires the resolution of relative short waves in large computational volumes. In the case of aircraft engines, for example, the frequencies of interest may require a grid spacing of roughly one centimeter and a corresponding computational cell volume of one cubic centimeter. Since modern engines have volumes of several cubic meters, a computational aeroacoustic simulation must involve millions of equations.

Acoustics problems are often posed in an infinite domain, but a computational domain must be finite. The computational domain is made finite by the introduction of a computational boundary condition on it's arbitrarily-located surface within the infinite domain. Most computational boundary conditions for these surfaces are local differential operators which presume some knowledge of the wave field in the neighborhood of the boundary surface, [1], [2].

If the surface is far from the sources of sound, this is a good approximation because theoretical acoustics gives a good estimate of the direction of wave propagation. But moving the bounding surface away from the sources makes the computional problem large. Reducing the size of the computational problem by moving the boundary surface close to the sources introduces errors because the complex wave fields near the source are incompatible with the assumptions used in the construction of the boundary conditions.

We are developing computational aeroacoustic boundary conditions which are valid for all wave fields, irrespective of their complexity. These boundary conditions may be applied close to the acoustic sources, so that the size of the computational volumes may be kept to a minimum. These conditions represent the superposition of all possible linear fields in the domain exterior to the computational volume. Since linearity is the only assumption about the exterior field, the computational volume may be reduced to the limit of this linear assumption. These boundary conditions are naturally more complicated because they contain more information. They are implemented as matrix or tensor operators and are called nonlocal boundary conditions because they represent the influence of a wave propagation between separate points on the boudary surface.

The first formulation and demonstration of these nonlocal boundary conditions was given in reference [3] for the case of wave propagation in a two-dimensional duct. There, it was shown that the computational space could be reduced by a factor of ten with no effect on the solution. A comparison of the nonlocal boundary condition with some local boundary conditions in reference [4] showed that the nonlocal conditions were accurate for all source fields, whereas the local conditions were sometimes accurate and sometimes inaccurate.

The purpose of this paper is to extend the formulation of reference [3] to the case of a three-dimensional sound field. Again, we use a rectangular duct so that the boundary surface is a simple plane. Because we must consider interactions between all pairs of points on this boundary surface, the boundary condition is a tensor operator.

The following section describes the problem in detail. Then the tensor boundary condition is derived for the case of a semi-infinite duct. This is followed by a discrete formulation and solution process for the Helmholtz (wave) equation with the nonlocal boundary condition. Computational results are given for several point sources oscillating at both low and high frequencies, and these results are compared to computations from convergent series solutions.

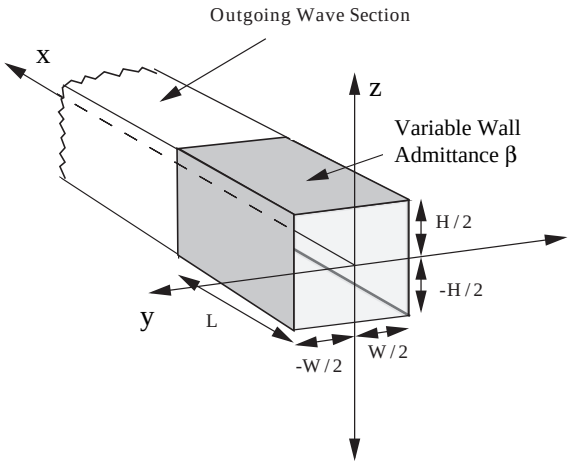

Figure 1. Semi-infinite duct geometry.

2 Problem Description

We wish to demonstrate the utility of a nonlocal boundary condition on a simple three-dimensional acoustics problem with a known solution. To this end, we consider the semi-infinite rectangular duct shown in figure 1. We want to find the numerical solution of the Helmholtz equation with a monopole source:

$$\nabla^2 \hat{p} + k^2 \hat{p} = \hat{s} \tag{1}$$

with local admittance boundary conditions on the entrance boundary plane, at $x = 0$, and on the side walls. These local admittance boundary conditions have the form

$$\hat{v}_n = \frac{1}{\bar{\rho}\bar{c}} \hat{\beta} \hat{p} + \hat{v}_s \tag{2}$$

where $\bar{\rho}$ and $\bar{c}$ are the ambient density and sound speed, respectively. This problem arises in duct acoustics and has a series solution. Physically, $\hat{p}$ is the complex acoustic pressure in the duct, and $k = \omega/\bar{c}$, where ω is the frequency of the disturbance. That is,

$$\hat{p}(\vec{x}, t) = \hat{p}(\vec{x}) e^{-\imath \omega t} \tag{3}$$

where $\imath$ is the unit complex number $\sqrt{-1}$. The physical side conditions are specified by the *local dimensionless admittances* β, and a *nonlocal admittance radiation condition* will be utilized on the surface $x = L$. This nonlocal boundary condition is derived from the following two constraints:

1. The general solution in the "outgoing wave" section ($x \geq L$), including the boundary ($x = L$), can be given as a series of radiating acoustic modes, or eigenfunctions, which satisfy the side wall boundary conditions.

2. The solution and its derivative with respect to x are continuous across the computational boundary plane ($x = L$), as required by the axial component of the momentum equation and by the continuity equation at the boundary plane.

For the problem considered here, these conditions lead directly to a natural nonlocal boundary condition.

Real duct problems are neither semi-infinite or likely to be limited to a finite set of modes, given an arbitrary source, so that the boundary condition will be only approximate. However, the intention here is to formulate a discrete boundary condition suitable for coupling with an internal discretization. In finite discretizations, only a finite number of modes are possible, and the discrete boundary condition will couple naturally with the interior discretization. Note that in an experimental setting, data at a radiation boundary are naturally described in terms of exterior modes and we show that this boundary condition is also useful in a numerical setting.

The discrete radiation boundary condition is a tensor equation of the form

$$\hat{u}_{jk} = \frac{1}{\bar{\rho}\bar{c}} \hat{\beta}_{jkj'k'} \hat{p}_{j'k'} + \hat{u}_{sjk} \tag{4}$$

where $\hat{p}_{j'k'}$ is the complex pressure at grid point (j', k'), $\hat{u}_{jk}$ is the axial velocity at grid point (j, k), and repeated indices are summed (Einstein summation notation) over the *finite* range of integers j and k. The index s refers to the source position, while all other indices are related to the numerical grid. For example, they correspond to samples of the pressure and axial velocity at grid points y_j and z_k on planes where x is constant. Boundary condition (4) is a generalization of the two-dimensional nonlocal boundary condition developed in reference [3]. Reference [4] showed that this nonlocal boundary condition is more accurate than several other local boundary conditions in the two-dimensional case.

The nonlocal boundary condition is computationally more expensive than local boundary conditions; however, section 4 provides evidence that the nonlocality is necessary to specify a proper physical interface between the computational domain and the exterior domain at an arbitrary boundary plane in a duct. Local boundary conditions involve some assumptions about the waves and their direction of propagation at the boundary. They do not permit general wave fields in the exterior domain.

The three-dimensional discretization of the Helmholtz equation with the nonlocal boundary conditons results in a large, sparse non-Hermitian matrix equation for the pressures in the computational domain. The matrix dimension for the higher frequency problems was of order 10^5. Because of the structure and large size of this matrix, attempts at solutions with direct methods were unsuccessful in the high-frequency cases. Solutions were attempted with two iterative, nonstationary Krylov subspace techniques: the QMR and TFQMR methods outlined in section 4. These iterative methods succeeded after the matrix was preconditioned. These techniques proved to be quite robust and are used to get the results shown in section 5.

3 Tensor Admittance Boundary Condition

Assume that at the boundary plane $x = L$ the velocity data are linearly related to the pressure data by an admittance tensor

$$\hat{u}(L, y_j, z_k) = \frac{1}{\bar{\rho}\bar{c}} \hat{\beta}_{jkj'k'} \hat{p}(L, y_{j'}, z_{k'}) \tag{5}$$

where $\hat{u}$ is the axial velocity and $\hat{p}$ is the pressure. The tensor $\beta_{jkj'k'}$ will be referred to as the *nodal admittance tensor*. In general, the tensor β depends on the *general solution* in the *exterior domain*. We may, for example, specify that the exterior solution is composed only of modes that describe rightward moving waves in the duct in figure 1. In many practical instances, known analytic forms of the exterior solution exist. Radiating modes from an infinite duct will be used here for analysis.

Note that calculation of the modes is not an explicit part of the solution scheme even though they are used to construct the boundary condition tensor $\hat{\beta}_{jkj'k'}$. This construction is done *only once* in advance of any calculations in the computational domain, and the boundary condition data are read or linked into the computational solution scheme. The following section gives a detailed formulation of the nonlocal admittance tensor for the infinite three-dimensional duct radiation condition.

3.1 Infinite Three-Dimensional Duct Radiation Condition

Modal solutions to rectangular-duct acoustic equations are

$$\hat{p}^{\pm}_{mn}(x, y, z) = \bar{\rho}\bar{c}^2 \phi_{mn}(y, z) e^{\pm \imath k_{xmn}(x-L)} \tag{6}$$

The function $\phi_{mn}(y, z)$ is the mode function and the time factor $e^{-\imath\omega t}$ is understood. Further, the sign of the imaginary part of the complex axial wavenumber k_{xmn} is positive. The mode function is defined by

$$\begin{aligned}
\phi_{mn}(y, z) &= \chi_m(y)\psi_n(z) && (7)\\
\chi_m(y) &= a_m e^{+\imath k_{ym} y} + b_m e^{-\imath k_{ym} y} && (8)\\
\psi_n(z) &= c_n e^{+\imath k_{zn} z} + d_n e^{-\imath k_{zn} z} && (9)\\
k_{xmn} &= \sqrt{k^2 - (k_{ym}^2 + k_{zn}^2)} && (10)
\end{aligned}$$

where eigenvalues k_{ym} and k_{zn} are computed with the methods in appendix A and the modal constants are computed using the methods of appendix B. In the simplest case of a hard-walled duct, $k_{ym} = m\pi/H$ and $k_{zn} = n\pi/W$. In soft-walled ducts, these eigenvalues are complex variables.

The pressure and velocity in a field of progressive waves in the infinite duct for $(x \geq L)$ is

$$\begin{aligned}
\hat{p}(x, y, z) &= \bar{\rho}\bar{c}^2 \sum_{m,n=0}^{\infty} \mathcal{P}^{+}_{mn} \phi_{mn}(y, z) e^{+\imath k_{xmn}(x-L)} && (11)\\
\hat{u}(x, y, z) &= \bar{c} \sum_{m,n=0}^{\infty} \mathcal{U}^{+}_{mn} \phi_{mn}(y, z) e^{+\imath k_{xmn}(x-L)} && (12)
\end{aligned}$$

where $\mathcal{P}^{+}_{mn}$ and $\mathcal{U}^{+}_{mn}$ are arbitrary constants that represent the modal pressure and velocity amplitudes. This solution is the general wave field solution in the exterior domain. The

axial momentum equation gives an alternate formula for the velocity

$$\hat{u}(x,y,z) = \bar{c} \sum_{m,n=0}^{\infty} \left(\frac{k_{xmn}}{k} \right) \mathcal{P}^{+}_{mn} \phi_{mn}(y,z) e^{+\imath k_{xmn}(x-L)} \tag{13}$$

Consistency of the two formulas requires that the velocity and pressure coefficients be related by

$$\mathcal{P}^{+}_{mn} = \left(\frac{k}{k_{xmn}} \right) \mathcal{U}^{+}_{mn} \tag{14}$$

The constants of proportionality are called the modal impedances $\mathcal{Z}_{mn}$:

$$\mathcal{Z}_{mn} = \left(\frac{k}{k_{xmn}} \right) \tag{15}$$

With these modal impedances, the proportionality of pressure and velocity is expressed as

$$\mathcal{P}^{+}_{mn} = \mathcal{Z}_{mn} \, \mathcal{U}^{+}_{mn} \tag{16}$$

The above impedance formula is a special adaptation of a general formula that relates the coefficients of any source-free wave field.

$$\mathcal{P}_{mn} = \sum_{m',n'=0}^{\infty} \mathcal{Z}_{mnm'n'} \, \mathcal{U}_{m'n'} \tag{17}$$

Equation (17) is a general *modal impedance* boundary condition that can represent any linear homogeneous boundary condition for the duct. It can also represent radiation effects at the end of a finite duct. The modal boundary condition that represents radiation in an infinite duct is recovered from the general formula with the definition

$$\mathcal{Z}_{mnm'n'} = \left(\frac{k}{k_{xmn}} \right) \delta_{mm'} \delta_{nn'} \tag{18}$$

where $\delta_{mm'}$ is the Kronecker delta. The general modal formulas for the pressure and velocity at the plane $x = L$ are, then,

$$\hat{p}(L,y,z) = \bar{\rho} \bar{c}^2 \sum_{m,n=0}^{\infty} \phi_{mn}(y,z) \sum_{m',n'=0}^{\infty} \mathcal{Z}_{mnm'n'} \, \mathcal{U}_{m'n'} \tag{19}$$

$$\hat{u}(L,y,z) = \bar{c} \sum_{m,n=0}^{\infty} \phi_{mn}(y,z) \, \mathcal{U}_{mn} \tag{20}$$

3.2 Nodal Impedance Boundary Condition

Modal solutions to duct acoustic problems are effective when the duct is uniform or has a finite number of uniform sections joined together [5]. In regions where the duct is highly nonuniform, general numerical methods are needed. Examples of nonuniform regions are transitions around centerbodies and sections that contain turbomachinery. Numerical methods applied to these regions need boundary conditions expressed in terms of the data structures of the method—typically, the values of the dependent variables at grid points, or *nodes*, of the numerical method. Assuming that the dependent variables are pressure and velocity

and that the acoustic field exterior to the computational domain is defined by linear equations, then a linear relation must exist between these variables on the boundary surface, which is part of both the interior, or computational, domain and the exterior linear domain. With a two-dimensional surface grid of points (y_j, z_k), the most general linear homogeneous relation between pressure and velocity over the grid of nodes is called the *nodal impedance* $Z_{jkj'k'}$:

$$\hat{p}_{jk} = \bar{\rho}\bar{c} \sum_{i',j'=1} Z_{jkj'k'} \hat{u}_{j'k'} \tag{21}$$

Exterior *sources* may be included by adding an inhomogeneous term to the above equation:

$$\hat{p}_{jk} = \bar{\rho}\bar{c} \sum_{i',j'=1} Z_{jkj'k'} \hat{u}_{j'k'} + \hat{p}_{sjk} \tag{22}$$

The unspecified summation ranges in the *nodal impedance* formulas are finite. We assume a rectangular computation grid with $1 \le j \le J$, $1 \le k \le K$ for simplicity. The points y_j, z_k are taken to be equally spaced with intervals $\Delta y, \Delta z$. These assumptions can be relaxed; however, this step adds nothing to the general implementaton here.

A relationship clearly exists between the *modal impedance* and the *nodal impedance*. The relation is made explicit by utilizing the *nodal velocities* to solve for the *modal velocity coefficients* and placing the resulting solution in an expression for the *nodal pressures*. The solution, in its simplest form, requires an equal number of *modes* and *nodes* in each coordinate dimension.

One-dimensional data structures are needed for the two-dimensional arrays. At a fixed axial location $(x = L)$, a vector of *nodal* velocities is defined by

$$\hat{u}_{jk} = \hat{u}(L, y_j, z_k) \tag{23}$$

$$\{\, \hat{u}_{jk} \,\} = \{\, \{\, \hat{u}_k \,\}_j \,\} \tag{24}$$

where the second script, k, varies through its range before the first script j is incremented. The vector on the left side of equation (23) is a column vector of column vectors. A similar structure is adopted for the *nodal* pressures:

$$\hat{p}_{jk} = \hat{p}(L, y_j, z_k) \tag{25}$$

$$\{\, \hat{p}_{jk} \,\} = \{\, \{\, \hat{p}_k \,\}_j \,\} \tag{26}$$

The *nodal* velocities are related to the *modal* velocity coefficients through the finite matrix approximation of the infinite sum in equation (20):

$$\{\, \hat{u}_{jk} \,\} = \bar{c}\, [\phi_{jkmn}]\, \{\, \mathcal{U}_{mn} \,\} \tag{27}$$

$$\phi_{jkmn} = \phi_{mn}(y_j, z_k) \tag{28}$$

In the above matrix, the first two scripts, jk are row dependent and the second two scripts are column dependent.

The *modal* velocity coefficients are given by a matrix inversion

$$\{\, \mathcal{U}_{mn} \,\} = \bar{c}^{-1}\, [\phi_{jkmn}]^{-1}\, \{\, \hat{u}_{jk} \,\} \tag{29}$$

Now, the *nodal pressure* is the finite matrix approximation to the infinite sum of equation (19):

$$\begin{aligned} \{\, \hat{p}_{jk} \,\} &= \bar{\rho}\bar{c}^2\, [\phi_{jkmn}]\, [\mathcal{Z}_{mnm'n'}]\, \{\, \mathcal{U}_{m'n'} \,\} \\ &= \bar{\rho}\bar{c}\, [\phi_{jkmn}]\, [\mathcal{Z}_{mnm'n'}]\, [\phi_{j'k'm'n'}]^{-1}\, \{\, \hat{u}_{j'k'} \,\} \end{aligned} \tag{30}$$

Consequently, the *nodal impedance* is given by the following similarity transformation of the *modal impedance*:

$$[Z_{jkj'k'}] = [\phi_{jkmn}]\,[\mathcal{Z}_{mnm'n'}]\,[\phi_{j'k'm'n'}]^{-1} \tag{31}$$

This result gives the desired *nodal impedance* relation between pressure and velocity:

$$\{\,\hat{p}_{jk}\,\} = \bar{\rho}\bar{c}\,[Z_{jkj'k'}]\,\{\,\hat{u}_{j'k'}\,\} \tag{32}$$

3.3 Nodal Admittance Boundary Condition

Other boundary conditions are readily formed with the nodal impedances. For example, a Helmholtz solver that utilizes only pressure as the dependent variable would require a relation between the pressure and the pressure gradient on the bounding surface. This relation must be nonlocal in order to be completely general.

In the present case of a duct for which the computational domain is bounded by the plane $x = L$, the axial momentum equation gives the axial velocity as

$$\{\,\hat{u}_{jk}\,\} = -\frac{\imath}{\bar{\rho}\bar{c}k}\left\{\,\tfrac{\partial \hat{p}(y_j,z_k)}{\partial x}\,\right\} \tag{33}$$

The pressure gradient and pressure are then related by

$$\left\{\left(\tfrac{\partial \hat{p}}{\partial x}\right)_{jk}\right\} = \imath k\,[\beta_{jkj'k'}]\,\{\,\hat{p}_{j'k'}\,\} \tag{34}$$

where the *nodal admittance* matrix is the inverse of the *nodal impedance* matrix:

$$[\beta_{jkj'k'}] = [Z_{jkj'k'}]^{-1} \tag{35}$$

This *nodal admittance* matrix is clearly a similarity transformation of a modal admittance matrix. Elements of this *modal admittance* matrix for an infinite duct would be the inverse of the elements in equation (18). Let the *modal admittance* be defined as the inverse of the *modal impedance* as shown:

$$[\mathcal{B}_{mnm'n'}] = [\mathcal{Z}_{mnm'n'}]^{-1} \tag{36}$$

The radiation condition for an infinite uniform duct is

$$\mathcal{B}_{mnm'n'} = \left(\frac{k_{xmn}}{k}\right)\delta_{mm'}\delta_{nn'} \tag{37}$$

The *nodal admittance* is a similarity transformation of the *modal admittance*:

$$[\beta_{jkj'k'}] = [\phi_{jkmn}]\,[\mathcal{B}_{mnm'n'}]\,[\phi_{j'k'm'n'}]^{-1} \tag{38}$$

3.4 Tensor Product Transformations

The matrices that define the boundary condition transformations become large for high-frequency computations. If we have a duct lateral dimension of $2^3 = 8$ wavelengths and the same number of points per wavelength in the computation, then each dimension requires $2^6 = 64$ grid points. The impedance and admittance matrices would have a dimension of $2^{12} = 4096$. Direct inversion should be avoided for these large matrices. Fortunately, the matrices in the boundary conditions are tensor products so that the computations are done separately for each dimension with the simplifications of the tensor product identities. These identities are given here to show the explicit computation procedures.

The similarity matrix can be written as

$$[\phi_{jkmn}] = [\chi_{jm}[\psi_{kn}]] \tag{39}$$
$$[\chi_{jm}] = [\chi_m(y_j)] \tag{40}$$
$$[\psi_{kn}] = [\psi_n(z_k)] \tag{41}$$

The similarity matrix $[\phi_{jkmn}]$ is formed with blocks of the matrix $[\psi_{kn}]$ scaled by elements of the matrix $[\chi_m(y_j)]$. Tensor product notation for this form is

$$[\phi_{jkmn}] = [\chi_{jm}] \otimes [\psi_{kn}] \tag{42}$$

In this notation, the second matrix supplies the block that is scaled by an element of the first matrix. With this convention, the inverse of the tensor product is the tensor product of the inverses, taken in the same order:

$$[\phi_{jkmn}]^{-1} = [\chi_{jm}]^{-1} \otimes [\psi_{kn}]^{-1} \tag{43}$$

The admittance and impedance matrices transform a vector into another vector. Let x, y be $(N \times 1)$ matrices and A be an $(N \times N)$ matrix. The transformation $y = Ax$ then takes N multiplications per row and N additions per row, assuming y is initially zero. Thus, a single transformation has $2N^2$ operations. The admittance transformation is

$$\{\,\{u\}\,\} = [\chi] \otimes [\psi]\,[\mathcal{B}]\,[\chi]^{-1} \otimes [\psi]^{-1}\,\{\,\{p\}\,\} \tag{44}$$

Each subvector is an $(N \times 1)$ matrix, and each sub-block matrix is an $(N \times N)$ matrix. The transformation can proceed from right to left. The first operation is to multiply $[\psi]^{-1}$ times each of the N subvectors $\{p\}$. This step requires $2N^3$ operations, and returns N subvectors. The next operation is to take linear combinations of these subvectors with the elements of each row of the matrix $[\chi]^{-1}$ as coefficients. This step also requires $2N^3$ operations and produces a vector of N^2 elements. Premultiplication of this vector by the diagonal matrix $[\mathcal{B}]$ requires N^2 operations. Each of the next two operations takes $2N^3$ operations, so that the total number of operations is $8N^3 + N^2$ for each transformation. By contrast, the full form of the matrix transformation would require $2(N^2)^2 = 2N^4$ operations. The tensor product form is superior to the expanded form for computation with iterative techniques. The tensor product is also superior for storage. Each matrix has N^2 elements, so that the total storage is $5N^2$ words. The expanded form of the transformation would use N^4 words.

4 The Discrete System

The discrete system represents the Helmholtz equation and all boundary conditions in discrete form. The Laplacian operator in three dimensions is represented by a seven-point stencil as follows:

$$\nabla^2 \hat{p}_{ijk} = \sum_{i'j'k'=-1}^{1} a_{i'j'k'} \hat{p}_{i+i',j+j',k+k'} \tag{45}$$

where the stencil data $a_{i'j'k'}$ depend on the algorithm that is implemented. Data for the second-order-accurate central-difference scheme are

$$a_{0,0,0} = -2\left(\frac{1}{\Delta x^2} + \frac{1}{\Delta y^2} + \frac{1}{\Delta z^2}\right) \tag{46}$$

$$a_{\pm 1,0,0} = \frac{1}{\Delta x^2} \tag{47}$$

$$a_{0,\pm 1,0} = \frac{1}{\Delta y^2} \tag{48}$$

$$a_{0,0,\pm 1} = \frac{1}{\Delta z^2} \tag{49}$$

where Δx, Δy, and Δz are the grid spacings in the respective dimensions.

Local admittance boundary conditions on the "entrance plane" and sidewalls are all taken in the form of equation (2). The momentum equations for the x, y, and z directions are

$$\frac{\partial \hat{p}}{\partial x} + \imath k \bar{\rho} \bar{c} \hat{u} = 0 \tag{50}$$

$$\frac{\partial \hat{p}}{\partial y} + \imath k \bar{\rho} \bar{c} \hat{v} = 0 \tag{51}$$

$$\frac{\partial \hat{p}}{\partial z} + \imath k \bar{\rho} \bar{c} \hat{w} = 0 \tag{52}$$

If we combine equations with the local admittance boundary conditions on the entrance and side walls, then we obtain

$$\frac{\partial \hat{p}_{1,j,k}}{\partial x} - \imath k \bar{\rho} \bar{c} \beta_{0,j,k} \hat{p}_{1,j,k} = -\imath k \bar{\rho} \bar{c} \hat{u}_{sjk}, \quad 1 \le j \le J, \quad 1 \le k \le K \tag{53}$$

$$\frac{\partial \hat{p}_{i,1,k}}{\partial y} - \imath k \bar{\rho} \bar{c} \beta_{-H/2,i,k} \hat{p}_{i,1,k} = 0, \quad 1 \le i \le I, \quad 1 \le k \le K \tag{54}$$

$$\frac{\partial \hat{p}_{i,J,k}}{\partial y} + \imath k \bar{\rho} \bar{c} \beta_{+H/2,i,k} \hat{p}_{i,J,k} = 0, \quad 1 \le i \le I, \quad 1 \le k \le K \tag{55}$$

$$\frac{\partial \hat{p}_{i,j,1}}{\partial z} - \imath k \bar{\rho} \bar{c} \beta_{-W/2,i,j} \hat{p}_{i,j,1} = 0 \quad 1 \le i \le I, \quad 1 \le j \le J \tag{56}$$

$$\frac{\partial \hat{p}_{i,j,K}}{\partial z} + \imath k \bar{\rho} \bar{c} \beta_{+W/2,i,j} \hat{p}_{i,j,K} = 0 \quad 1 \le i \le I, \quad 1 \le J \le J \tag{57}$$

A discrete *nonlocal admittance* boundary condition, as described in the previous section, is used on the exit plane $x = x_I = L$.

$$\frac{\partial \hat{p}_{I,j,k}}{\partial x} = \imath k \beta_{j,k,j',k'} \hat{p}_{I,j',k'} \tag{58}$$

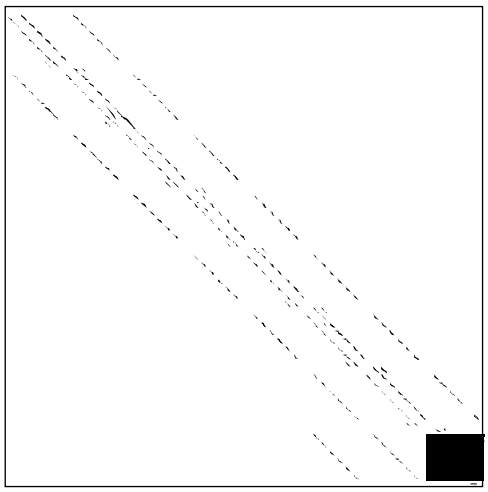

Figure 2. Sparse matrix from the linear system. Nonzero elements are indicated by dark marks. The block in the lower right corner is generated by the nonlocal boundary condition.

The sum in equation (58) is over the entire y-z grid at the boundary. Forward or backward difference formulas were utilized at the computational domain surfaces to avoid the introduction of "ghost points."

The three-dimensional array of unknowns $p_{i,j,k}$ is arranged as a column matrix, where the indices i, j, and k vary in reverse order with their position; that is, k varies first, then j varies, and then i varies last.

$$\{\, \hat{p}_{ijk} \,\} = \hat{p}_(x_i, y_j, z_k) = \{\, \{\, \{\, \hat{p}_k \,\}_j \,\}_i \,\} \tag{59}$$

$$\{\, \hat{u}_{ijk} \,\} = \hat{u}_(x_i, y_j, z_k) = \{\, \{\, \{\, \hat{u}_k \,\}_j \,\}_i \,\} \tag{60}$$

Major partitions of this column of unknowns are based on the axial index i. Each partition is a column matrix that contains the unknown pressures on a single cross-sectional plane. Subpartitions of these columns are based on the y-dimension index j. These subpartitions define column matrices for which only the z-dimension index k varies.

The system matrix is the square coefficient matrix of the above column of unknowns. Its nonzero elements are the coefficients from the difference operator (45)–(49), the local boundary conditions (53)-(57), and the nonlocal admittance boundary condition (58). The system matrix is very sparse (most of its elements are zero) because the Helmholtz equation is a local operator; however, a significant block of $(J \times K)$ nonzero elements exists due to the nonlocal boundary condition. Figure 2 is a graphic illustration of the system matrix structure. This system matrix is clearly sparse, except for the large data block in the lower right corner where the coefficients for the nonlocal boundary condition are stored.

Direct solutions to the above system matrix were attempted and found to be impractical, at least for workstation calculations. Banded matrix solvers could not be used because they fill the inner null bands of the sparse matrix with nonzero elements. With matrix dimensions $O\,[10^5]$, the matrix bandwidth would be $O\,[10^3]$, and a banded solver would create $O\,[10^8]$ elements. Consequently, the iterative QMR and TFQMR techniques described below were selected to solve the discrete system matrix equation. These methods are known as Krylov subspace techniques. Further details on these techniques can be found in references [6], [7], and [8]. In accordance with the recommendation of Freund, [9], the Krylov subspace techniques were applied to the system matrix in its complex form. Otherwise, when a complex system of dimension N is written as a real system of dimension $2N$, then a matrix may be produced with a distribution of eigenvalues that includes the origin or values very

near the origin. A matrix with such values is singular or nearly singular and can present difficulties for the QMR and TFQMR Krylov subspace techniques.

4.1 Preconditioning Concepts

In some cases, the system matrix equation could not be solved with the iterative techniques without the application of *preconditioning*. This preconditioning was necessary for convergence of the iteration (not just for acceleration of the rate of convergence). In other cases that could be solved without preconditioning, the preconditioning accelerated the rate of convergence. Thus, preconditioning was always beneficial.

The notion of preconditioning is a simple. Instead of solving the original system $Ax = b$, an equivalent system $A'x' = b'$ is solved, where $A' = PAQ$, $x' = Q^{-1}x$, and $b' = Pb$. The equivalent system must be constructed such that the matrix A' has more desirable properties than the original matrix A. An example of a more desirable property is an improved matrix condition number, which makes the equivalent system amenable to solution by iterative techniques.

If an invertable matrix can be chosen in factored form $M = M_1 M_2$, then the elements of the equivalent preconditioned system $A'x' = b'$ are of the form

$$A' = {M_1}^{-1} A {M_2}^{-1}, \qquad b' = {M_1}^{-1} b, \qquad x' = M_2 x \tag{61}$$

The corresponding Krylov subspace technique generates in a translated subspace,

$$x'_n \in x'_0 + \mathcal{K}_n(r'_0, A') \tag{62}$$

where $\mathcal{K}_n(r'_0, A') = \text{span}\{r'_0, A'r'_0, A'^2 r'_0, \cdots, A'^{n-1} r'_0\}$. In terms of the original system, Krylov iterates x_n and residuals $r_n = b - Ax_n$ are connected by

$$x_n = {M_2}^{-1} {x'}_n \in x_0 + \mathcal{K}_n(M^{-1} r_0, M^{-1} A) \text{ and } r_n = M_1 {r'}_n \tag{63}$$

For minimum residual techniques, the *right* preconditioning matrix $M_2 = I$ is the identity. This identity matrix is generally preferred so that the preconditioned residual is the same as the ordinary residual.

The more common preconditioners are reviewed in reference [10]. The choice of preconditioners used here was influenced more by their availability than by a detailed evaluation of their suitability for the problem at hand. The ones used here were members of a general class of preconditioners that are implemented within the software package *qmrpack* [11].

4.2 Methods of Preconditioning

Two preconditioning methods were found that worked effectively. These methods were the Symmetric Successive Overrelaxation (SSOR) method and the Incomplete Gaussian Elimination (ILU) method. These methods are described more fully below.

4.2.1 SSOR Method

The SSOR method is an interative technique for solving a linear system $Ax = b$. The matrix A is written as $D - E - F$, where D, E, and F are the diagonal, strict lower triangular, and strict upper triangular portions of A, respectively. For the classic Successive Overrelaxation (SOR) technique, a parameter ω, which is the *overrelaxation parameter*, is introduced and $Ax = b$ is rewritten as

$$(D - \omega E)x - [(1 - \omega)D + \omega F]\, x = \omega b \tag{64}$$

An iterative method is produced by letting the leftmost x be the new iterate $u^{(m+1)}$ and the rightmost x be the old iterate $u^{(m)}$:

$$(D - \omega E)u^{(m+1)} = [(1-\omega)D + \omega F]\, u^{(m)} + \omega b \tag{65}$$

or

$$u^{(m+1)} = (D - \omega E)^{-1}\, [(1-\omega)D + \omega F]\, u^{(m)} + (D - \omega E)^{-1}\omega b \tag{66}$$

The inverse is only slightly more expensive to compute than a matrix multiplication because the matrix is lower triangular.

The SSOR technique is a modification of the SOR technique in which the vector is modified from the top to the bottom and then from the bottom back up to the top to complete one iteration. The SSOR technique has the form

$$\begin{aligned} u^{(m+1/2)} &= (D - \omega E)^{-1}\, [(1-\omega)D + \omega F]\, u^{(m)} + (D - \omega E)^{-1}\omega b \\ u^{(m+1)} &= (D - \omega F)^{-1}\, [(1-\omega)D + \omega E]\, u^{(m+1/2)} + (D - \omega E)^{-1}\omega b \end{aligned} \tag{67}$$

Written in one step, SSOR is an iteration $u^{(m+1)} = Mu^{(m)} + f$, where

$$M = I - \omega(2\omega - 1)(D - \omega F)^{-1} D (D - \omega E)^{-1} A \tag{68}$$

and f is a fixed vector that may be worked out from (67). The idea in any iterative technique is to minimize M in some way (usually by minimizing the spectral radius). Ideally, $M = 0$ so that the inversion can be accomplished in one step. If M is "small," then $(D - \omega F)^{-1} D (D - \omega E)^{-1}$ is a good approximate inverse of A (modulo a constant multiplier); moreover, because of the triangular form of its factors, it is easily computed. This matrix M is the preconditioner in the SSOR technique.

4.2.2 ILU Method

The ILU method has variants that are designated by ILU(n), where n is an integer. The idea that underlies the basic ILU(0) preconditing is taken from Gaussian elimination. First, find an upper triangular matrix U and lower triangular L such that $A = LU$. The ILU preconditioning contains a remainder term $A = LU + R$ and imposes a constraint on the structure of $L + U$ (i.e., $L + U$ must have nonzero elements within the envelope in which A has nonzero elements). The remainder term results because fill-in is not allowed at elements of L and U that were already zero. With this constraint, the underlying matrix-vector multiplication with the preconditioned matrix is no more expensive than when applied to the original matrix A. The ILU(0) may be extended by allowing additional inward fill in L and U, which leads to the ILU(p) algorithms, where p is the maximum inward fill. Further details of the ILU(0) algorithm and its variants may be found in [10].

Numerical experiments with both preconditioning methods showed that they were effective in accelerating the rates of convergence of the iterative solutions. The ILU method was found to be more reliable for this problem; however, so that it was adopted to prepare the results shown in the following section.

5 Results

This section contains the results of numerical solution of the discrete system outlined in section 4. The computationally less difficult results are presented first and the more difficult results are presented later. The higher frequencies and more complicated sources present increased difficulties. Two types of sources are specified at the inlet boundary that represent opposite extremes: a plane wave source and a point source. The source conditions are specified as

$$\frac{\partial \hat{p}_{1,j,k}}{\partial x} = \hat{v}_{sjk} \qquad 1 \le j \le J, \quad 1 \le k \le K$$

If $\hat{v}_{sjk} = C$, where C is a complex constant, the source is a *plane wave source*. If $\hat{v}_{sjk} =$

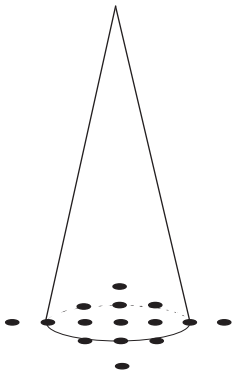

Figure 3. Approximate representation of the delta function by an inverted cone. Support of the cone extends over five grid points.

$C\ \delta(y - y_0, z - z_0)$, the source is a *point source*. Series solutions for both source boundary conditions are derived in appendix C. The delta-function source is not representable by a single continuous function or on a discrete grid. In the following numerical experiments, the truncated modal series was used to analytically represent the delta function. Similarly, an inverted cone of unit volume, such as the one in figure 3, was used to numerically represent the delta function.

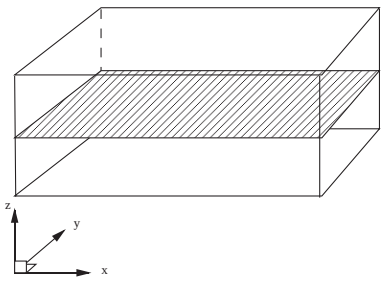

Figure 4. Duct computational domain. The shaded region indicates the horizontal plane on which pressure data are shown in subsequent plots.

The plotted results to be shown later are the complex pressure on a horizontal plane that cuts through the center of the duct as shown in figure 4. Some plots show the result of the application of the boundary condition at different locations in the duct. The purpose here is to show that the solution is fairly insensitive to the point of application of the boundary condition. In each computation, a uniform grid with equal grid spacing in each coordinate direction was used. The grid spacing was choosen to give a resolution of 10 points per wavelength.

5.1 Hard-Walled Duct with Plane Source

In a hard-walled duct, the admittance of each of the four side walls is identically zero. Plots of the real part of acoustic pressure are shown in Figure 5 for a planar source that oscillates at a frequency of 500 Hz. As expected, the acoustic pressure is independent of the spanwise direction and no evidence of any reflections from the radiation boundary is observed. The interior solution is in excellent agreement with the analytical solution on this scale. Real and imaginary parts of the acoustic pressure differed by a phase shift of 90°, so only the real part of the acoustic pressure is plotted here.

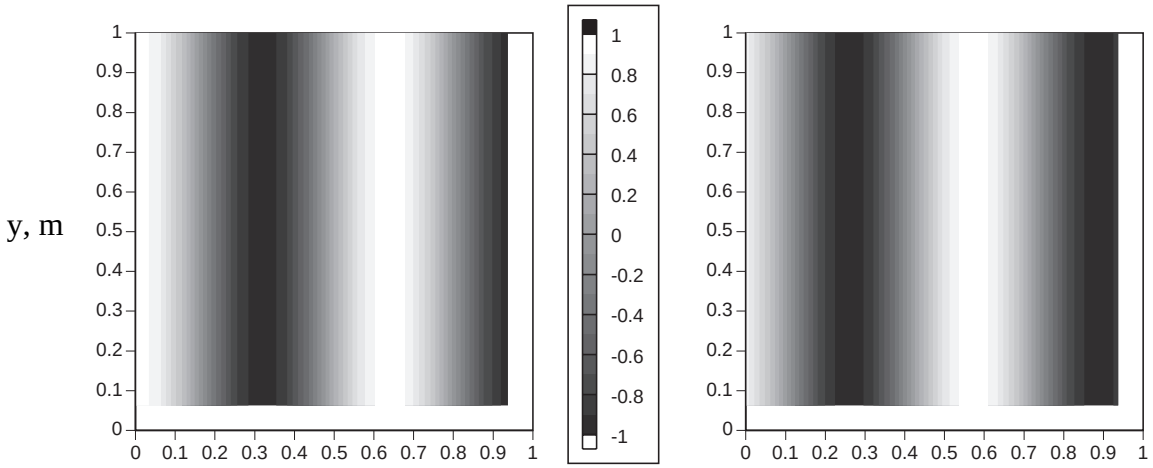

(a) Series. (b) Numerical.

Figure 5. Real part of the pressure field due to a 500 Hz plane-wave source in a hard-walled duct. Results computed with a $(17 \times 17 \times 17)$ grid in a 1.0 m cubic domain.

Figure 6 shows the results obtained for the real part of the acoustic pressure, where the frequency of the planar source has been increased to 1,000 Hz. Here, the number of grid points per meter was doubled, to accommodate the shorter wavelength, and the radiation boundary condition was applied at 0.5 m down the duct (preserving the total number of grd points). Results are consistent with those obtained at 500 Hz. Again, the imaginary part of the acoustic pressure was not plotted because it was identical to the real part, except for a phase shift of 90°.

5.2 Hard-Walled Duct with Point Source

To demonstrate that the solution is independent of the radiation boundary condition for all sources, a point source was used to generate the acoustic wave pattern in the hard wall duct. Point source calculations are a severe test of both the numerical method and radiation boundary condition. Classic modal analysis shows that eigenfunction components of the acoustic fields generated by point sources are of two types: modes that decay exponentially in space (cut-off modes) and modes that are purely periodic in space (cut-on modes). The real and imaginary parts of the acoustic pressure calculated for a point source that oscillates at 1,000 Hz are shown in figures 7 and 8 respectively. The radiation boundary condition was applied 1.0 m from the source. Several cut-on modes generate a complicated pressure pattern away from the source. Near the radiation boundary, the acoustic pressure field, computed from the numerical method, is identical to the modal series results. However, in

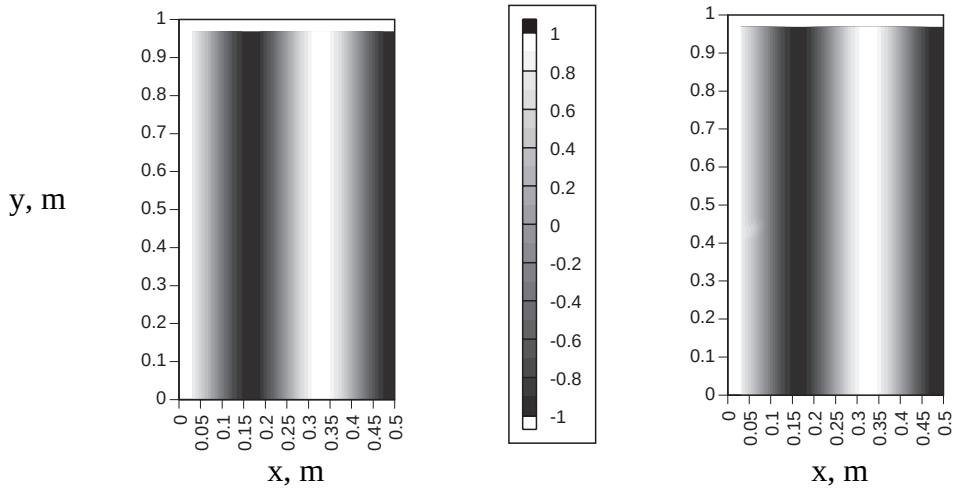

Figure 6. Real part of the pressure field due to a 1000 Hz plane-wave source in a hard-walled duct. Results computed with a $(17 \times 33 \times 33)$ grid in a section with axial dimension of 0.5 m.

the vicinity of the point source, the imaginary part of the acoustic pressure computed from the modal series and the numerical method show a discrepancy. The discrepancy between the numerical method and modal series in the vicinity of the point source was expected. Near the source plane, a large number of duct modes and, hence, grid points are needed to represent the acoustic point source. Thus, the discrepancy near the source is believed to be caused by the coarseness of the grid near the source.

To further investigate the discrepancy in the computed acoustic field near the point source at 1,000 Hz, numerical results were obtained when the radiation boundary was moved to 0.5 m from the source. These results are shown in figures 9 and 10.

Note that the movement of the radiation boundary closer to the source had little or no effect on the acoustic pressure field computed by the numerical method. This result lends further credence to the hypothesis that the discrepancy near the source is due to the coarseness of the grid (because the grid spacing was not changed when the radiation boundary was moved closer to the source). The basic solution process would be expected to work on an uneven grid; however, this case was not tested.

For point sources that oscillate at frequencies above 1000 Hz, the combined effect of many cut-on and cut-off modes generates a pattern that indicates multidirectional wavefronts that would not be captured with simpler local-plane-wave type of boundary conditions. Numerical results are plotted in figures 11 and 12 for a point source that oscillates at 1,500 Hz. The radiation boundary condition was applied at 1.0 m from the source. Again, a discrepancy can be observed in the imaginary part of the pressure in the vicinity of the point source. When the radiation boundary is placed at 0.5 m from the source (figures 13 and 14, this discrepancy is still present.

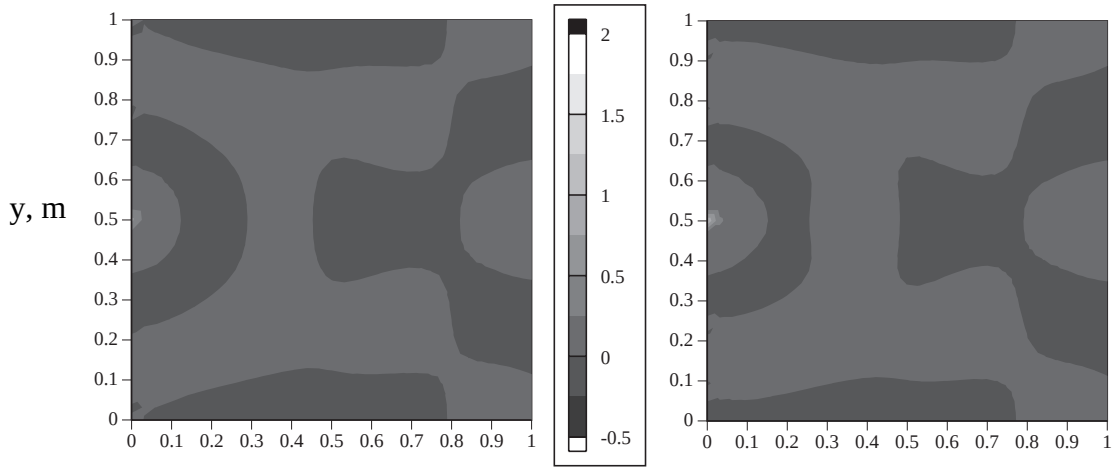

(a) Series. (b) Numerical.

Figure 7. Real part of the pressure field due to a 1000 Hz point source in a hard-walled duct. Nonlocal boundary condition applied at 1.0 m. Results computed with a $(33 \times 33 \times 33)$ grid.

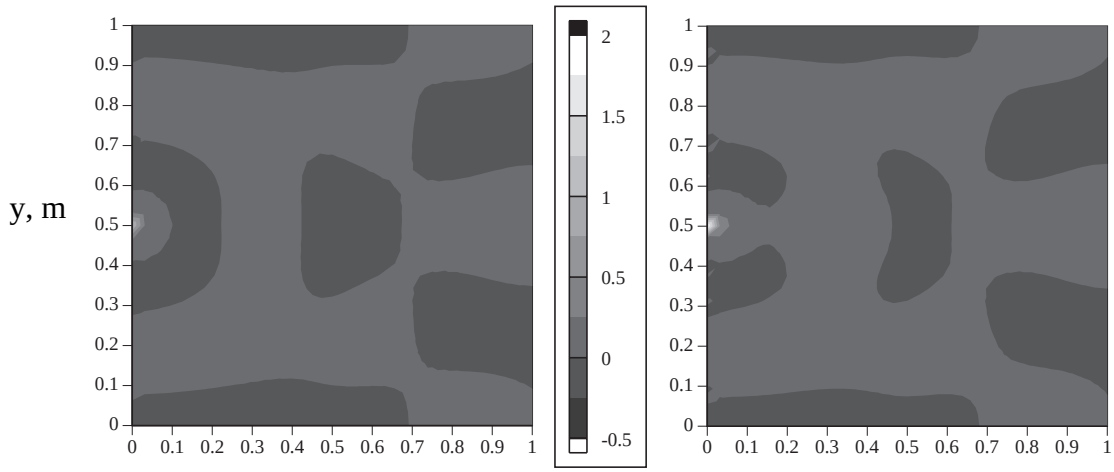

(a) Series. (b) Numerical.

Figure 8. Imaginary part of the pressure field due to a 1000 Hz point source in a hard-walled duct. Nonlocal boundary condition applied at 1.0 m . Results computed with a $(33 \times 33 \times 33)$ grid.

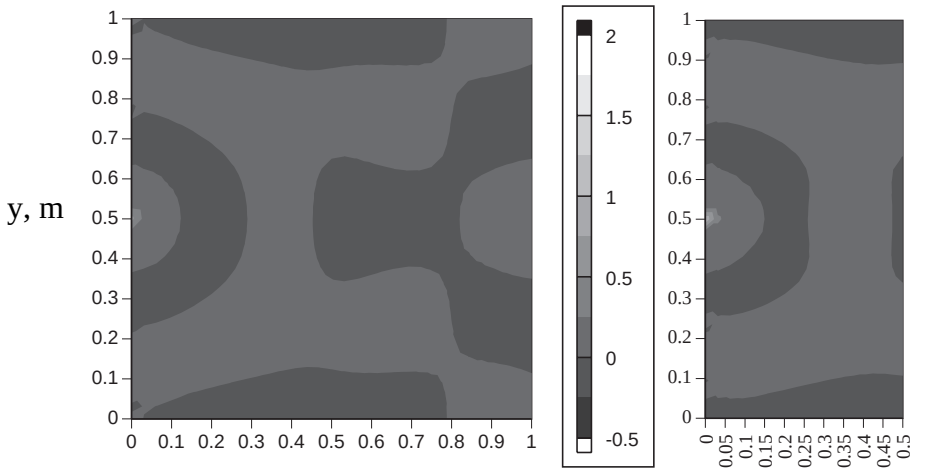

Figure 9. Real part of the pressure field due to a 1000 Hz point source in a hard-walled duct. Nonlocal boundary condition applied at 0.5 m. Results computed with a $(17 \times 33 \times 33)$ grid.

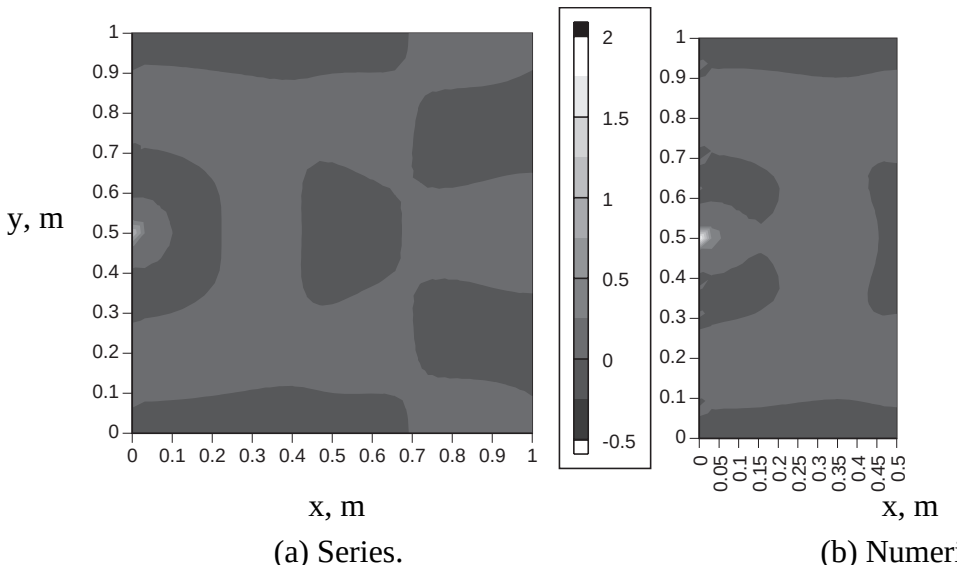

Figure 10. Imaginary part of the pressure field due to a 1000 Hz point source in a hard-walled duct. Nonlocal boundary condition applied at 0.5 m. Results computed with a $(17 \times 33 \times 33)$ grid.

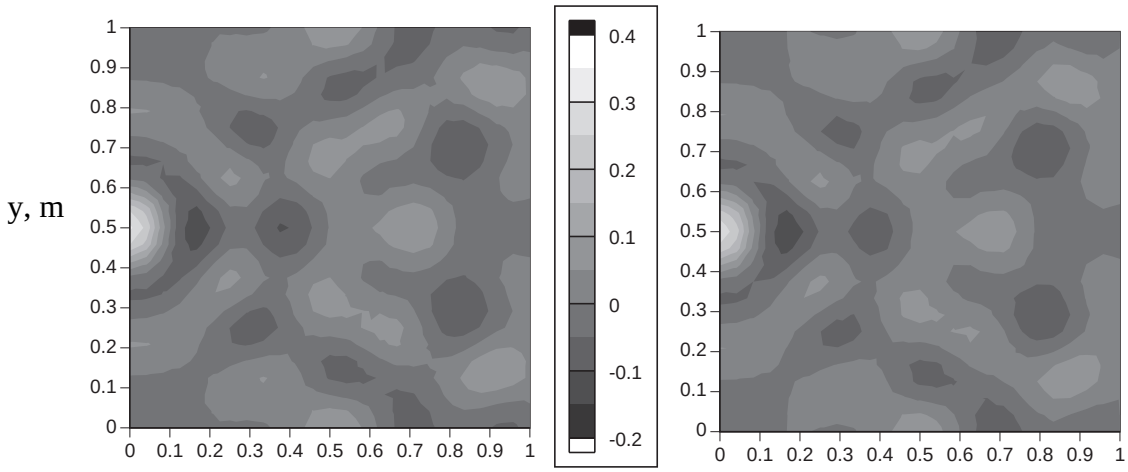

(a) Series. (b) Numerical.

Figure 11. Real part of the pressure field due to a 1500 Hz point source in a hard-walled duct. Nonlocal boundary condition applied at 1.0 m. Results computed with a $(49 \times 49 \times 49)$ grid.

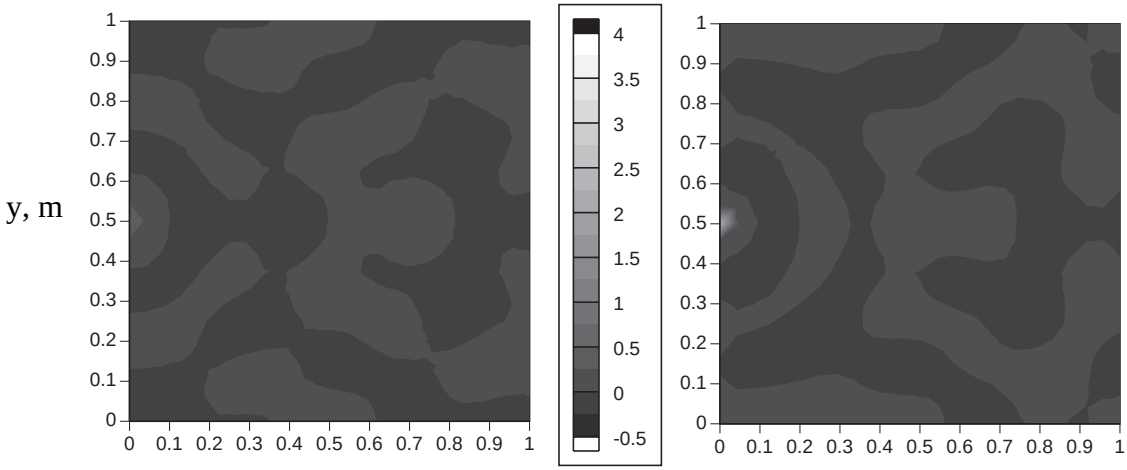

(a) Series. (b) Numerical.

Figure 12. Imaginary part of the pressure field due to a 1500 Hz point source in a hard-walled duct. Nonlocal boundary condition applied at 1.0 m . Results computed with a $(49 \times 49 \times 49)$ grid.

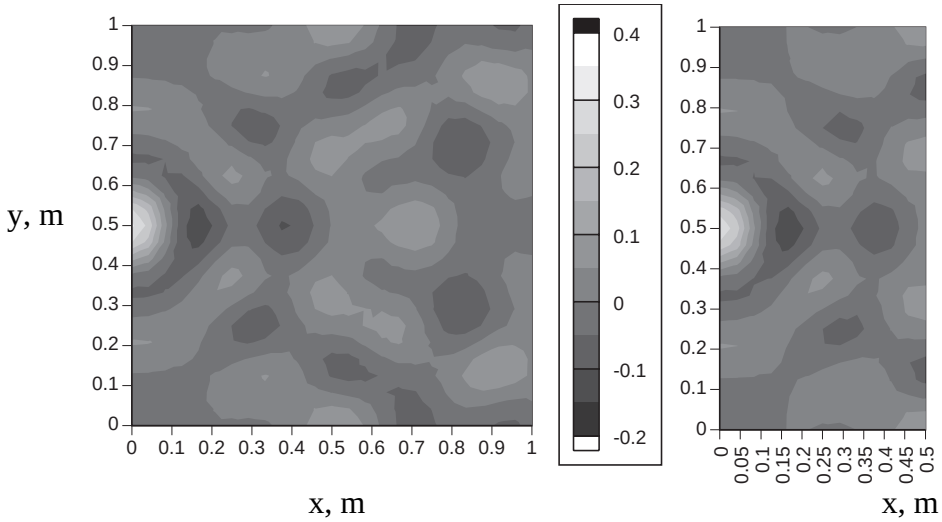

(a) Series. (b) Numerical.

Figure 13. Real part of the pressure field due to a 1500 Hz point source in a hard-walled duct. Nonlocal boundary condition applied at 0.5 m. Results computed with a $(25 \times 49 \times 49)$ grid.

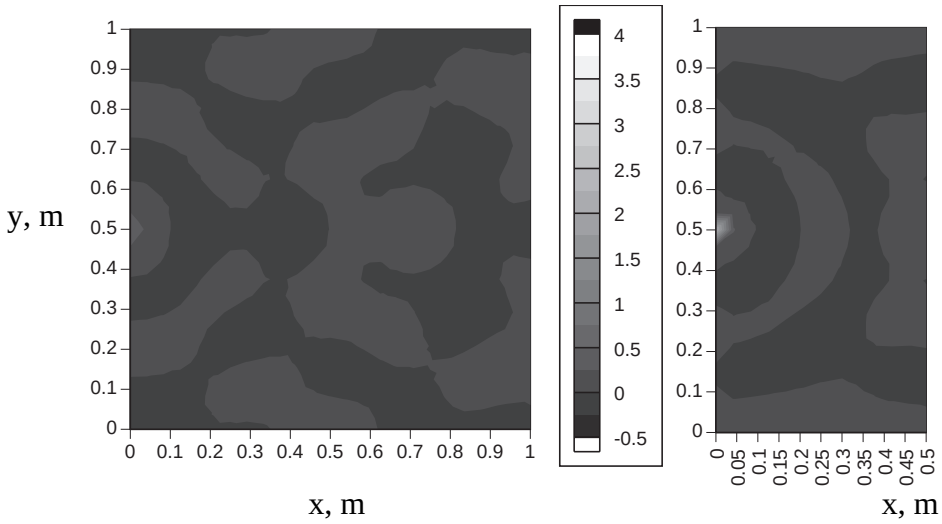

(a) Series. (b) Numerical.

Figure 14. Imaginary part of the pressure field due to a 1500 Hz point source in a hard-walled duct. Nonlocal boundary condition applied at 0.5 m. Results computed with a $(25 \times 49 \times 49)$ grid.

5.3 Soft-Walled Duct with Point Source

The radiation condition has also been tested with acoustically treated, or soft, walls. In contrast to hard-walled ducts, acoustically treated ducts have surfaces that are not perfectly reflecting. Results for the soft-walled duct case were computed with the admittance $\beta = .5 - .5i$ in equation (2). Acoustically treated walls damp out acoustic disturbances and reduce the number of contributing waves compared with the hard-walled case. To limit the number of graphs, results for the soft-walled duct are only presented for the more-troublesome point source.

Figures 15 through 18 show the results of a point source that oscillates at 1,000 Hz in the soft-walled duct. Figures 15 and 16 show results for the radiation boundary located 1.0 m from the source; figures 17 and 18 show results for the radiation boundary located at 0.5 m from the point source. On this scale, the numerical solution is not affected by the distance of the radiation boundary from the point source. The discrepancy that occurred in the imaginary part of the acoustic pressure for hard-walled ducts is not observed in the lined duct. This difference is believed be caused by the fact that the lining has a damping effect on the acoustic waves and also reduces the number of contributing waves in comparison with to those in the rigid-walled duct. The agreement between the results for the numerical solution and modal series is excellent. Reflections from the nonlocal radiation boundary condition are not evident at this frequency.

Figures 19 through 22 show results of a 1500 Hz point source that oscillates in the lined duct. Significant damping of the acoustic waves is clearly observed, in comparison with the corresponding results for the hard-walled duct. The conclusions drawn from this set of plots are consistent with those for 1,000 Hz.

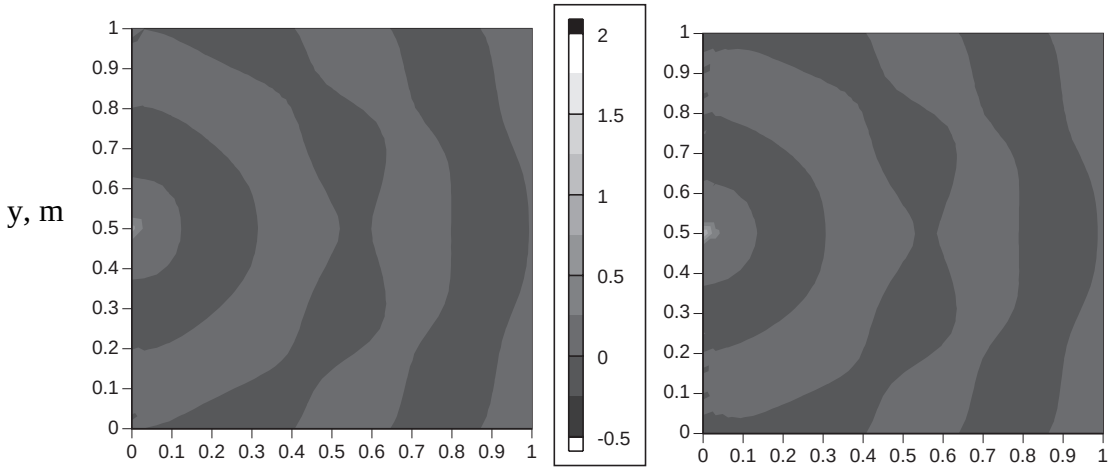

Figure 15. Real part of the pressure field due to a 1000 Hz point source in a soft-walled duct. Nonlocal boundary condition applied at 1.0 m. Results computed with a $(33 \times 33 \times 33)$ grid.

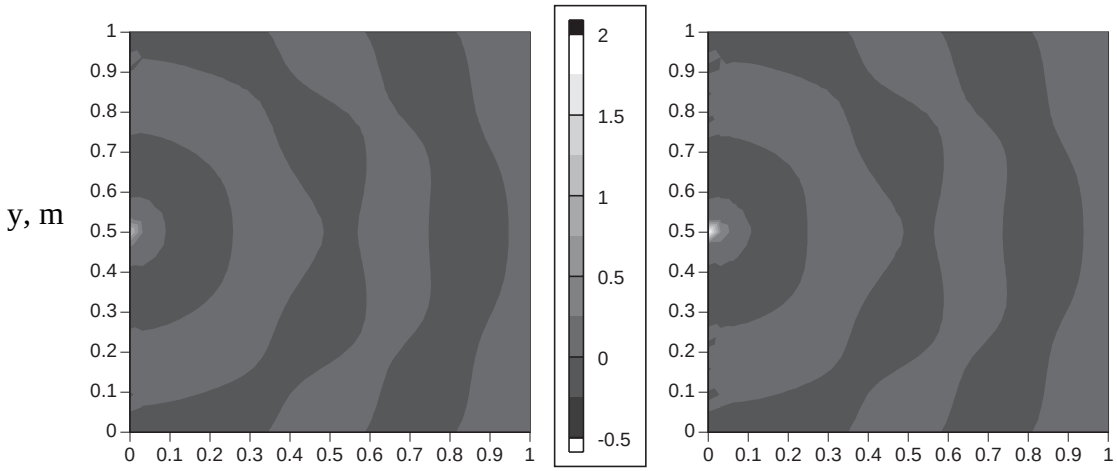

Figure 16. Imaginary part of the pressure field due to a 1000 Hz point source in a soft-walled duct. Nonlocal boundary condition applied at 1.0 m. Results computed with a $(33 \times 33 \times 33)$ grid.

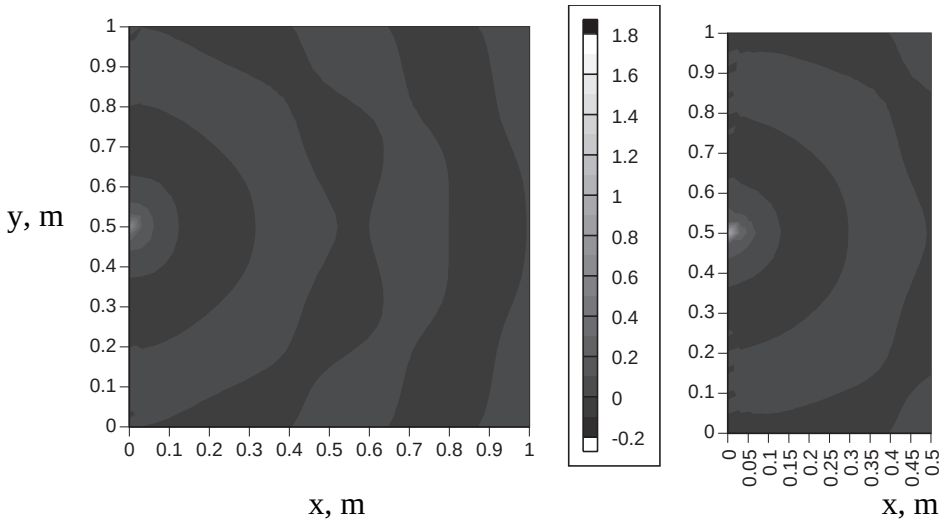

(a) Series. (b) Numerical.

Figure 17. Real part of the pressure field due to a 1000 Hz point source in a soft-walled duct. Nonlocal boundary condition applied at 0.5 m. Results computed with a $(17 \times 33 \times 33)$ grid.

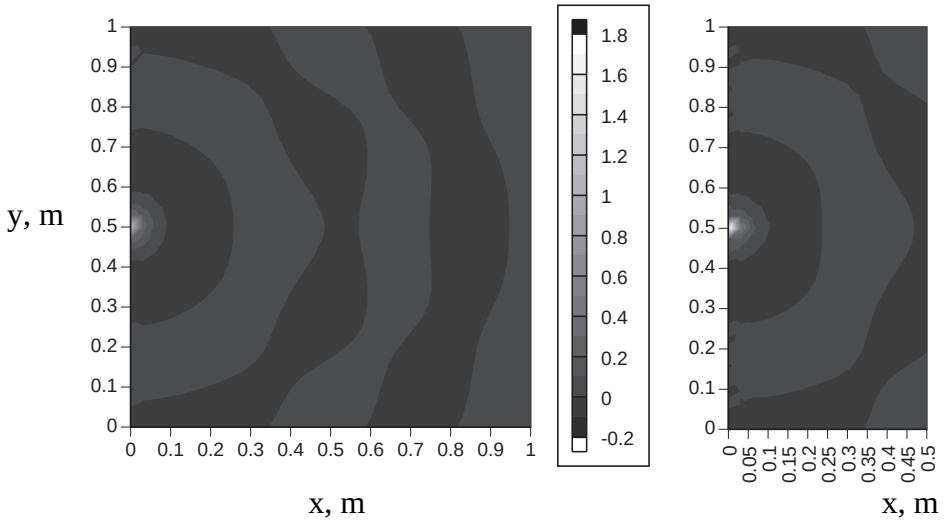

(a) Series. (b) Numerical.

Figure 18. Imaginary part of the pressure field due to a 1000 Hz point source in a soft-walled duct. Nonlocal boundary condition applied at 0.5 m. Results computed with a $(17 \times 33 \times 33)$ grid.

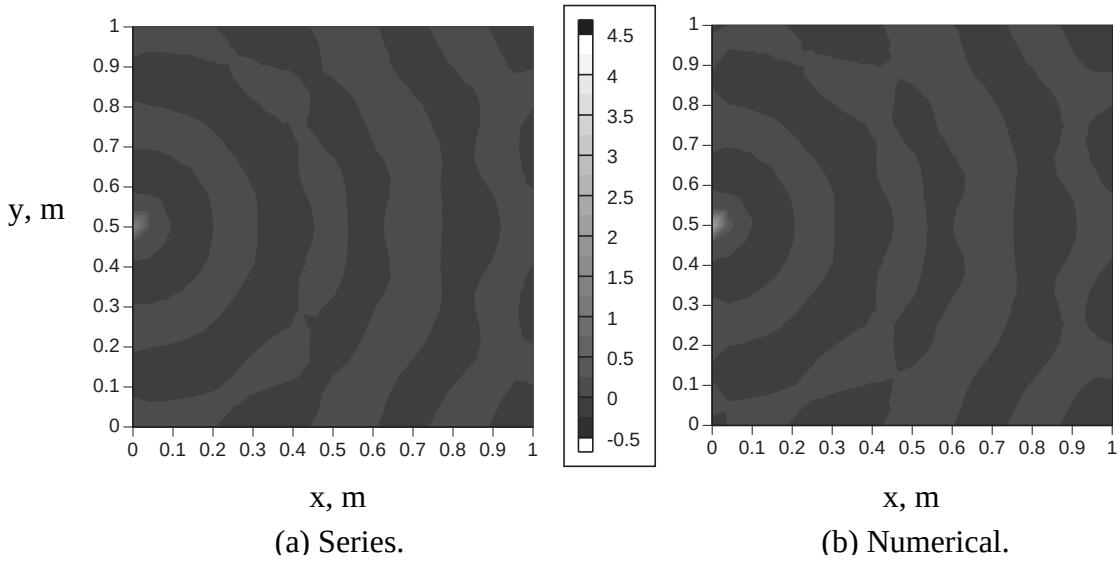

Figure 19. Real part of the pressure field due to a 1500 Hz point source in a soft-walled duct. Nonlocal boundary condition applied at 1.0 m . Results computed with a $(49 \times 49 \times 49)$ grid.

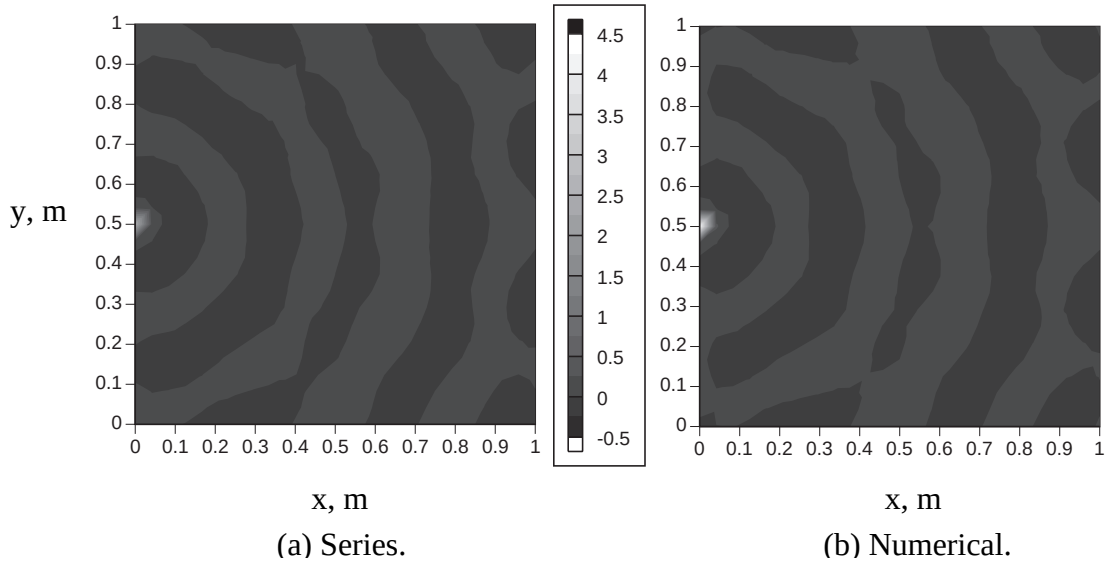

Figure 20. Imaginary part of the pressure field due to a 1500 Hz point source in a soft-walled duct. Nonlocal boundary condition applied at 1.0 m. Results computed with a $(49 \times 49 \times 49)$ grid.

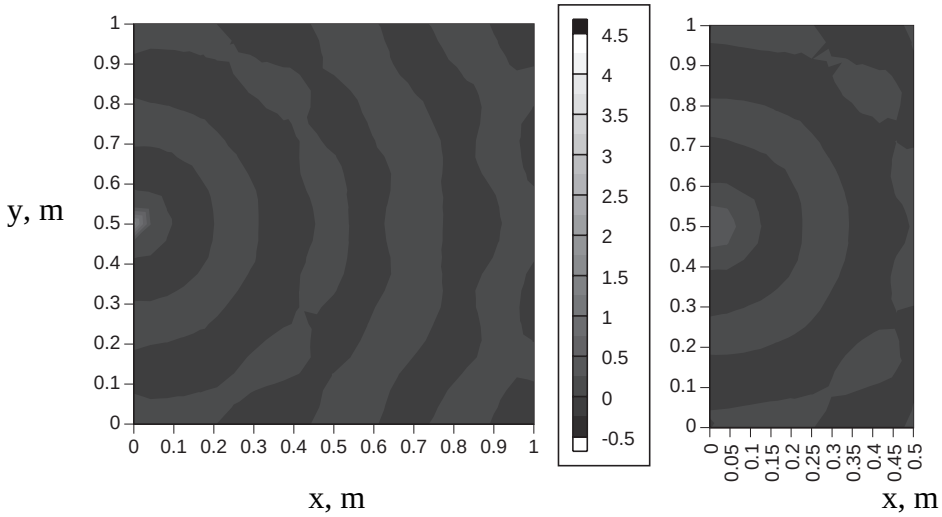

Figure 21. Real part of the pressure field due to a 1500 Hz point source in a soft-walled duct. Nonlocal boundary condition applied at 0.5 m. Results computed with a $(25 \times 49 \times 49)$ grid.

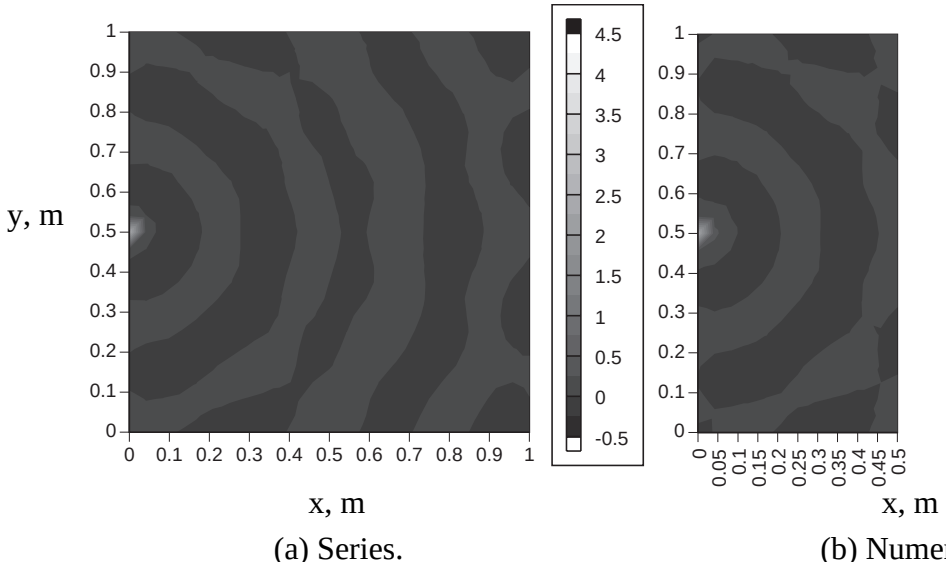

Figure 22. Imaginary part of the pressure field due to a 1500 Hz point source in a soft-walled duct. Nonlocal boundary condition applied at 0.5 m. Results computed with a $(25 \times 49 \times 49)$ grid.

6 Concluding Remarks

A nonlocal boundary condition has been formulated for the Helmholtz equation in three-dimensional Cartesian coordinates. The boundary condition represents the nonreflection condition on a cross-sectional plane within a semi-infinite rectangular duct. This boundary condition is completely independent of the wave field and transmits waves from any source distribution without perceptible reflection. The boundary plane can be moved close to the source without affecting the solution for the wave field.

In order to demonstrate the boundary condition, a three-dimensional system of finite-difference equations was written to model acoustic waves generated by arbitrary sources in a semi-infinite duct with the Helmholtz equation. Source conditions were prescribed at the entrance plane, and conventional local boundary conditions were used on the duct sidewalls. The nonlocal boundary condition was applied on the exit or end plane of the duct, which defines the extent of the computational domain. On this end plane, which can be placed at an arbitrary position, the acoustic field must be the same as the field within a semi-infinite duct with an arbitrary source distribution.

The resulting system of equations was large and sparse. In order to solve this system for practical frequencies for which the duct dimensions were many multiples of the wavelength, two types of preconditioning were investigated. These two methods were Symmetric Successive Over-relaxation (SSOR) preconditioning and Incomplete Gaussian Elimination (ILU) preconditioning. The ILU method was found to be more reliable for this problem. System solutions were found with ILU preconditioning and Krylov subspace iterative schemes.

To assess the effectiveness of the nonlocal boundary condition, numerical solutions were compared with classical series solutions. The physical model used in the comparison was a duct that measured $1\,m \times 1\,m$ in cross section. The duct was semi-infinite, but the computational domain was closed at the arbitrarily located right end by the nonlocal boundary condition. Comparisons were made for two different source types (i.e., plane waves and point sources) at the left end. Comparisons were also made for both hard and absorbing side walls. Computations were made for 500, 1,000, and 1,500 Hz at standard atmospheric conditions to generate complex sound fields. Within this context, the closing boundary was moved to various positions to verify that the predicted sound field was invariant to its location. In all cases, the boundary location had no perceptible effect on the predicted sound field. The numerically predicted field matched the field produced by the series solution with a high degree of accuracy. Because the boundary condition represents the exterior domain general solution, it can be used to obtain computional solutions for irregular interior domains when classic series solutions are not available.

These examples demonstrate that nonlocal boundary conditions on the surface of a three-dimensional computational domain can accurately represent the effect of a surrounding infinite domain on the acoustic solutions within the finite computational domain. Because the solutions are invariant to the location of the computational boundary, the nonlocal boundary conditions provide a means of minimizing the size of the computational domain.

References

[1] Engquist, Bjorn; and Majda, Andrew: Absorbing Boundary Conditions for the Numerical Simulation of Waves. *Mathematics of Co mputations*, Vol 31, 1977, pp. 629–651.

[2] Giles, M. B.: Nonreflecting Boundary Conditions for Euler Equation Calculations. AIAA paper 89-1912, 1989.

[3] Zorumski, W. E.; Watson, W. R.; and Hodge, S. L.: A Non-Local Computational Boundary Condition for Duct Acoustics. NASA TM-109091, 1994.

[4] Watson, W. R.; Zorumski, W. E.; and Hodge, S. L.: Evaluation of Several Non-reflecting Computational Boundary Conditions for Duct Acoustics. NASA TM-109118, 1994.

[5] Zorumski, William E.: Acoustic Theory of Axisymmetric Multisectioned Ducts. NASA TR 419, 1974.

[6] Birkhoff, G.; and Lynch, R.: *Numerical Solution of Elliptic Problems.* Society for Industrial and Applied Mathematics, 1984.

[7] Press, W.; Flannery, B.; Teukolsky, S.; and Vetterling, W.: *Numerical Recipes in C.* Cambridge University Press, 1988.

[8] Strikwerda, J.: *Finite Difference Schemes and Partial Differential Equations.* Wadsworth Pub. Co., 1989.

[9] Freund, R.; Golub, G.; and Nachtigal, N.: Iterative Solutions of Linear Systems. *Acta Numerica,* Vol. 1, 1992, pp. 75–100.

[10] Saad, Y.: *Numerical Solution of Large Eigenvalue Problems.* Society for Industrial and Applied Mathematics, 1994.

[11] Freund, R.; and Nachtigal, M.: *Available by ftp via anonymous login to netlib.att.com in directory /linalg.*

A Eigenvalue Computation

A.1 High-Order Eigenvalues

When the walls are hard, the eigenvalues are multiples of π; when the walls have finite admittances, a complex characteristic equation must be solved for the eigenvalues. This step can easily be the most difficult part of the computation, so the method is developed here in considerable detail. We group the admittance β at the wall with the frequency parameter k and the height H by defining $\tau_0 \equiv \bar{\rho}\bar{c}\beta_0 kH$ and $\tau_H \equiv \bar{\rho}\bar{c}\beta_2$.

If we assume elementary solutions of the form $e^{\pm \imath k_y y}$ and apply admittance boundary conditions at the lower and upper walls, the following equation is obtained for the eigenvalues $k_y H$:

$$1 - e^{2\imath k_y H} \left(\frac{1 - \frac{\tau_H}{k_y H}}{1 + \frac{\tau_H}{k_y H}} \right) \left(\frac{1 - \frac{\tau_0}{k_y H}}{1 + \frac{\tau_0}{k_y H}} \right) = 0 \tag{69}$$

In the case of hard walls, where $\tau_0 = \tau_H = 0$, solutions to equation (69) are

$$k_y H = m\pi, \quad m = 0, 1, 2, \cdots \tag{70}$$

where δ_m is used here as a measure of the displacement of an eigenvalue from its nominal hard-walled position in the complex plane.

This elementary case suggests the definition

$$(k_y H)_m = m\pi + \delta_m, \quad m = 0, 1, 2, \cdots \tag{71}$$

A.1.1 Characteristic Equation for Higher Modes, $m > 0$

The characteristic equation for the higher modes can be given in logarithmic form as

$$\begin{aligned} F(\delta_m) &= \delta_m \\ &+ \frac{\imath}{2} \log \left[1 + \frac{\tau_0}{m\pi + \delta_m} \right] + \frac{\imath}{2} \log \left[1 + \frac{\tau_H}{m\pi + \delta_m} \right] \\ &- \frac{\imath}{2} \log \left[1 - \frac{\tau_0}{m\pi + \delta_m} \right] - \frac{\imath}{2} \log \left[1 - \frac{\tau_H}{m\pi + \delta_m} \right] \\ &= 0 \end{aligned} \tag{72}$$

This form of the characteristic equation shows clearly that the solution δ_m approaches zero in the limit where $m \to \infty$. The points at which $m\pi + \delta_m = \pm\tau_{0,H}$ are singularities of F that cannot be solutions. These points should not cause difficulty, except possibly in the case where $m = 0$. The explicit form of equation (72) is important. By computing each logarithim separately, we avoid crossing the branch cut, which may introduce an error of π in the value of the complex log.

A.1.2 Newton's Method for Solution of Higher Modes

Newton's method for solution of equation (72) utilizes an iteration for δ_m given by the replacement operation

$$\delta_m \leftarrow \delta_m - \frac{F(\delta_m)}{F'(\delta_m)} \tag{73}$$

where the derivative of the characteristic function is

$$F'(\delta_m) = 1 - \imath \frac{\tau_0}{(m\pi + \delta_m)^2 - \tau_0^2} - \imath \frac{\tau_H}{(m\pi + \delta_m)^2 - \tau_H^2} \tag{74}$$

This solution method is effective for higher modes ($m > 1$). One can quickly generate a thousand or more eigenvalues on a modern workstation. The work in developing a useful basis for a modal computation is limited then to computing the lower eigenvalues. This computation is discussed below.

A.2 Low-Order Eigenvalues

A.2.1 Alternate form of the characteristic equation

Newton's method is fast and dependable for the case in which $m > 1$; however, special care is needed for cases in which $m = 0$ or $m = 1$. The problem is worse when the admittances have large imaginary parts and small real parts, so we attack these cases first. In these cases, pure imaginary solutions may exist for the eigenvalue $k_y H$. Accordingly the following definitions are introduced to investigate these cases:

$$k_y H = -\imath\eta \tag{75}$$

$$a = -\tau_0 \tau_H \tag{76}$$

$$b = -\imath \frac{\tau_0 + \tau_H}{2} \tag{77}$$

These changes of variable allow the characteristic equation to be expressed as

$$F(\eta) = a + \eta^2 + 2b\eta \coth \eta = 0 \tag{78}$$

To this point, no real change has occurred, because all variables are complex. Now consider solutions in which the parameters a b are real variables (i.e., the real parts of the complex parameters defined above). We can find real solutions ξ for these real parameters and add the effects of their imaginary parts later.

A.2.2 Solutions for Real Parameters

Now take the real parts a_1 b_1 of the parameters $a = a_1 + \imath a_2$ and $b = b_1 + \imath b_2$. For brevity, we use the same symbols a b with the understanding that they are restricted to real values in this subsection. When the parameters are real, a better form of the characteristic equation utilizes the square of the eigenvalue as

$$\xi = \eta^2 = -(k_y H)^2 \tag{79}$$

$$F(\xi) = a + \xi + 2b \frac{C(\xi)}{S(\xi)} \tag{80}$$

$$C(\xi) \equiv \cosh \eta \tag{81}$$

$$S(\xi) \equiv \frac{\sinh(\eta)}{\eta} \tag{82}$$

The value of the characteristic function at the origin and its behavior when ξ is large are important for determining if the characteristic function has zeros for positive ξ.

$$F(0) = a + 2b \tag{83}$$

$$F(\xi) \sim \xi, \quad \xi \to \infty \tag{84}$$

The defined functions $C(\xi)$ and $S(\xi)$ have properties that make them useful in determining solutions to the characteristic equation. These properties will be listed here before considering the numerical procedure for solving for the eigenvalues.

The functions are defined by the series for the hyperbolic functions:

$$C(\xi) = \sum_{n=0}^{\infty} \frac{\xi^n}{(2n)!} \tag{85}$$

$$S(\xi) = \sum_{n=0}^{\infty} \frac{\xi^n}{(2n+1)!} \tag{86}$$

The series definitions permit the following immediate observations:

$$S(\xi) \leq C(\xi), \quad 0 \leq \xi < \infty \tag{87}$$

$$S'(\xi) \leq C'(\xi), \quad 0 < \xi < \infty \tag{88}$$

$$1 \leq C(\xi), \quad 0 \leq \xi < \infty \tag{89}$$

$$\frac{1}{2} \leq C'(\xi), \quad 0 \leq \xi < \infty \tag{90}$$

$$1 \leq S(\xi), \quad 0 \leq \xi < \infty \tag{91}$$

$$\frac{1}{6} \leq S'(\xi), \quad 0 \leq \xi < \infty \tag{92}$$

The following formulas are useful for evaluating the derivatives of the functions:

$$C'(\xi) = \frac{1}{2} S(\xi) \tag{93}$$

$$S'(\xi) = \frac{C(\xi) - S(\xi)}{2\xi} \tag{94}$$

Finally, the functions have the following asymptotic character:

$$S(\xi) \sim \xi^{-1/2} C(\xi), \quad \xi \to \infty \tag{95}$$

$$S'(\xi) \sim \frac{1}{2} \xi^{-1} C(\xi), \quad \xi \to \infty \tag{96}$$

$$C'(\xi) \sim \frac{1}{2} \xi^{-1/2} C(\xi), \quad \xi \to \infty \tag{97}$$

The first derivative of the characteristic function is

$$F'(\xi) = 1 + \frac{b}{S^2(\xi)} \left(\frac{C(\xi) S(\xi) - 1}{\xi} \right) \tag{98}$$

$$F'(0) = 1 + \frac{2}{3} b \tag{99}$$

$$F'(\xi) \sim 1 + b \xi^{-1/2}, \quad \xi \to \infty \tag{100}$$

The derivative $F'(\xi)$ approaches unity from above or below, depending on the sign of b when ξ is large. The derivative $F'(0)$ may be positive or negative, depending on the value of b; $F'(0)$ is positive for $b > -3/2$, zero for $b = -3/2$, and negative for $b < -3/2$. The second derivative of the characteristic function is

$$F''(\xi) = -\frac{b}{S^3(\xi)} \left[\frac{C(\xi)(S^2(\xi) - 2) + S(\xi)}{2\xi^2} \right] \tag{101}$$

$$F''(0) = -\frac{4}{45} b \tag{102}$$

$$F''(\xi) \sim -\frac{b}{2} \xi^{-3/2}, \quad \xi \to \infty \tag{103}$$

The function within brackets is positive, so that the sign of the second derivative depends only on the sign of b. If b is negative, then the curvature is positive; if b is positive, the curvature is negative. The limit of the function within brackets is $4/45$ for $\xi = 0$, which gives the value of the derivative at the origin.

Small solutions $|\xi| << 1$ are possible for certain combinations of the parameters a b. These combinations are identified by utilizing a two-term series for the characteristic function:

$$F(\xi) = F(0) + F'(0)\xi = 0 \tag{104}$$

which gives the following estimate for η^2

$$\xi = -\left(\frac{a+2b}{1+\frac{2}{3}b}\right) \tag{105}$$

In order for this estimate to be consistent with the assumed smallness of ξ, the parameters must be related by

$$-|F'(0)|\,\epsilon \le F(0) \le +|F'(0)|\,\epsilon \tag{106}$$

$$-\left|1+\frac{2}{3}b\right|\epsilon \le F(0) \le +\left|1+\frac{2}{3}b\right|\epsilon \tag{107}$$

In the special case for which $b \to -3/2$, the limits above show that $a \to -2b$. These solutions can be positive or negative because they represent the effect of the parameters in moving the solutions from the real K_yH axis to the imaginary K_yH axis in the neighborhood of the origin.

A long list of cases needs to be investigated in determining whether solutions for K_yH exist near the origin or on the imaginary axis (ξ is positive). The cases will be organized here by defining ranges of the characteristic function and its slope at the origin. These parameters ($F(0)$ and $F'(0)$) depend on the parameters a b only.

1. If $F'(0) > +\epsilon$, then the slope of the characteristic function is positive everywhere. If $F(0) > +\epsilon$, then no positive solution exists; however,
   (a) If $|F(0)| \le \epsilon$, then a small solution $\xi = O(\epsilon)$ exists, or else
   (b) else If $F(0) < -\epsilon$, then a positive solution $\xi > 0$ exists, or else
2. If $|F'(0)| \le \epsilon$, then the slope at the origin is near zero. If $F(0) > +\epsilon^2$, then no positive solution exists; however,
   (a) If $|F(0)| \le \epsilon^2$, then a small double solution $\xi = O(\epsilon)$ exists, or else
   (b) If $F(0) < -\epsilon^2$, then a positive solution exists, or else
3. If $F'(0) < -\epsilon$, then the slope at the origin is negative and the characteristic function has a minimum for some $\xi > 0$. Find the location of the minimum ξ_{min} and evaluate the characteristic function to get its minimum value F_{min}. If $F_{min} > \epsilon^2$, then no solution exists; however,
   (a) If $|F_{min}| \le \epsilon^2$, then a double solution exists near ξ_{min}, or else
   (b) If $F_{min} < -\epsilon^2$, then the solutions depend on the value of F at the origin.
      i. If $F(0) > +\epsilon^2$, then two distinct solutions $\xi < \xi_{min}$ and $\xi > \xi_{min}$ exist, or else
      ii. If $|F(0)| \le \epsilon^2$, then a solution near $\xi = 0$ exists and another solution $\xi > \xi_{min}$ exists, or else
      iii. If $F(0) < -\epsilon^2$, then a single solution $\xi > \xi_{min}$ exists.

A.2.3 Solutions for Complex Parameters

Now that we have found all possible solutions for real parameters, the next step is to find the effect of the imaginary parts of the parameters on these solutions. Let the parameters a b be complex functions of a real parameter s, which varies from zero to unity ($0 \leq s \leq 1$). The parameters are identical to their real parts when $s = 0$ and take their actual values when $s = 1$. Begin with the solutions for real parts of the parameters for the case in which $s = 0$ and trace these solutions to the point at which $s = 1$. Note that these solutions can include effects of the real parts of the admittances in the parameter a. The tracing follows a differential equation for the square of the eigenvalue $\xi(s)$ as a function of the parameter s:

$$K_y(s)H = \sqrt{-\xi(s)} \tag{108}$$

$$a = -\tau_0\tau_H \tag{109}$$

$$b = -i\frac{\tau_0 + \tau_H}{2} \tag{110}$$

$$a(s) = \Re[a] + i\Im[a]s = a_1 + ia_2 s \tag{111}$$

$$b(s) = \Re[b] + i\Im[b]s = b_1 + ib_2 s \tag{112}$$

Now, $\xi(s)$, $a(s)$, and $b(s)$ are complex functions of the real variable s. The characteristic function depends on s and is complex but is otherwise unchanged from the one defined for the real variables:

$$F(\xi;s) = a(s) + \xi + 2b(s)\frac{C(\xi)}{S(\xi)} \tag{113}$$

$$\frac{\partial F(\xi;s)}{\partial \xi} = 1 + b(s)\left(\frac{C(\xi)S(\xi) - 1}{\xi S^2(\xi)}\right) \tag{114}$$

$$\frac{\partial^2 F(\xi;s)}{\partial \xi^2} = -\frac{b(s)}{S^3(\xi)}\left[\frac{C(\xi)(S^2(\xi) - 2) + S(\xi)}{2\xi^2}\right] \tag{115}$$

$$\frac{\partial F(\xi;s)}{\partial s} = a'(s) + 2b'(s)\frac{C(\xi)}{S(\xi)} \tag{116}$$

The solutions for which $s = 0$ are initial conditions for a first-order differential equation, which is used to find $\xi(s)$:

$$d\xi = -\frac{\left(\frac{\partial F}{\partial s}\right)}{\left(\frac{\partial F}{\partial \xi}\right)}ds \tag{117}$$

This equation is valid as long as the initial condition is not a double eigenvalue. When the initial condition is a double eigenvalue ξ_m, the partial derivative in the denominator is

$$\frac{\partial F}{\partial \xi} = \frac{\partial^2 F(\xi;s)}{\partial \xi^2}(\xi - \xi_m) \tag{118}$$

The differential equation for ξ is then singular, but a differential equation for the square of the displacements of the eigenvalues from the double eigenvalue is not singular.

$$d(\xi - \xi_m)^2 = -2\frac{\left(\frac{\partial F}{\partial s}\right)}{\left(\frac{\partial^2 F}{\partial \xi^2}\right)}ds \tag{119}$$

Given an initial step Δs, the two eigenvalues near the double eigenvalue are

$$\xi = \xi_m \pm \sqrt{-2 \frac{\left(\frac{\partial F}{\partial s}\right)}{\left(\frac{\partial^2 F}{\partial \xi^2}\right)} \Delta s} \tag{120}$$

The differential equation for the eigenvalue is then used to trace each of these to the final value for $s = 1$.

B Acoustic Modes

The velocity and pressure due to a single acoustic mode are given by

$$k \left\{ \begin{array}{c} \hat{v} \\ \hat{p} \end{array} \right\} = \left[\begin{array}{cc} \bar{c} & 0 \\ 0 & \bar{\rho}\bar{c}^2 \end{array} \right] \left[\begin{array}{cc} k_y e^{\imath k_y y} & -k_y e^{-\imath k_y y} \\ k e^{\imath k_y y} & k e^{-\imath k_y y} \end{array} \right] \left\{ \begin{array}{c} a \\ b \end{array} \right\} \tag{121}$$

Admittance boundary conditions on the top and bottom walls are

$$\lfloor\, 1 \quad -\beta_t \,\rfloor \left\{ \begin{array}{c} \hat{v} \\ \hat{p} \end{array} \right\} = 0 \tag{122}$$

$$\lfloor\, 1 \quad +\beta_b \,\rfloor \left\{ \begin{array}{c} \hat{v} \\ \hat{p} \end{array} \right\} = 0 \tag{123}$$

We can combine these equations ot obtain a matrix equation for the modal constants:

$$\left[\begin{array}{cc} (k_y h - kh\beta_t) e^{+\imath k_y h/2} & -(k_y h + kh\beta_t) e^{-\imath k_y h/2} \\ (k_y h + kh\beta_b) e^{-\imath k_y h/2} & -(k_y h - kh\beta_b) e^{+\imath k_y h/2} \end{array} \right] \left\{ \begin{array}{c} a \\ b \end{array} \right\} = 0 \tag{124}$$

B.1 Ratio of Coefficients

Either of the above equations can be used to solve for the ratio a/b or b/a. The first gives

$$\left(\frac{b}{a}\right) = \frac{(k_y h - kh\beta_t)}{(k_y h + kh\beta_t)} e^{+\imath k_y h} \tag{125}$$

and the second gives

$$\left(\frac{a}{b}\right) = \frac{(k_y h - kh\beta_b)}{(k_y h + kh\beta_b)} e^{+\imath k_y h} \tag{126}$$

The product of these results is unity, which is the eigenvalue equation treated in appendix A. Here, however, we want only the ratio, with the assumption that the eigenvalue solution is complete. Because some error may occur in the eigenvalue calculation, we take the arithmetic average of the two solutions.

$$\left(\frac{b}{a}\right) = \frac{1}{2}\left[\left(\frac{b}{a}\right) + \left(\frac{a}{b}\right)^{-1} \right] \tag{127}$$

B.2 Normalization

Given the ratio of the coefficients, the magnitude of one coefficient (e.g. ,a) can now be chosen such that the average potential energy in the mode is unity. With the two-sided transform, the average potential energy is the average of the magnitude of the pressure. Consequently, we set

$$\frac{1}{H} \int_{-H/2}^{H/2} |\hat{p}|^2 \, dy = 1 \tag{128}$$

This condition determines the magnitude of a:

$$|a|^{-2} = \lfloor\, 1 \quad (b/a)^* \,\rfloor \left[\begin{array}{cc} \left\langle e^{\imath k_y y}, e^{\imath k_y y} \right\rangle & \left\langle e^{\imath k_y y}, e^{-\imath k_y y} \right\rangle \\ \left\langle e^{-\imath k_y y}, e^{\imath k_y y} \right\rangle & \left\langle e^{-\imath k_y y}, e^{-\imath k_y y} \right\rangle \end{array} \right] \left\{ \begin{array}{c} 1 \\ (b/a) \end{array} \right\} \tag{129}$$

where the inner product of two variables is defined as

$$\langle u, v \rangle = \frac{1}{H} \int_{-H/2}^{H/2} u^* v \, dy = 1 \tag{130}$$

The inner normalization condition determines the magnitude of a. A choice is still available for the phase. The convention will be used that the phase of the pressure is zero at $y = 0$:

$$\arg \hat{p}(0) = 0 \rightarrow \arg(a + b) = 0 \tag{131}$$

This choice is achieved by setting

$$\arg a = -\arg\left[1 + (b/a)\right] = 0 \tag{132}$$

B.3 Inner Products

The inner products needed are

$$\left\langle e^{ik_u y}, e^{ik_v y} \right\rangle = \left\langle 1, e^{i(k_v - k_u^*)y} \right\rangle = \frac{\sin\left(\frac{(k_v - k_u^*)H}{2}\right)}{\left(\frac{(k_v - k_u^*)H}{2}\right)} = \text{sinc}\left(\frac{(k_v - k_u^*)H}{2}\right) \tag{133}$$

The sinc function is defined with a limiting case

$$\text{sinc}\, z = \begin{cases} \frac{\sin z}{z} & \text{if } |z| > 0 \\ 1 - \frac{1}{6}z^2 & \text{if } |z| \rightarrow 0 \end{cases} \tag{134}$$

C Series Solutions of the Helmholtz Equation

C.1 Inner Products

The inner product of two functions is defined as

$$\langle u, v \rangle = \frac{1}{\mathcal{D}} \int_{\mathcal{D}} u^* v \, d\mathcal{D} \tag{135}$$

where $\mathcal{D}$ indicates the domain of the functions. In one dimension, $|\mathcal{D}|$ is the length of the interval; and, in two dimensions, it is the area. Because the first variable is conjugated, the average of a product over space is

$$\overline{uv} = \langle u^*, v \rangle \tag{136}$$

The average of the magnitude squared of a complex function is

$$\overline{|u|^2} = \langle u, u \rangle \tag{137}$$

and the average of the square of a function is

$$\overline{u^2} = \langle u^*, u \rangle \tag{138}$$

The average of a squared function is complex, but the average of the magnitude squared is real.

The inner product of two modes is defined as

$$\langle \phi_{mn}(y,z), \phi_{m'n'}(y,z) \rangle = \frac{1}{HW} \int_{-W/2}^{+W/2} \int_{-H/2}^{+H/2} \phi^*_{mn}(y,z) \phi_{m'n'}(y,z) \, dy \, dz \tag{139}$$

where the domain is HW. Because the two-dimensional modes are products of one-dimensional modes,

$$\langle \phi_{mn}, \phi_{m'n'} \rangle = \langle \chi_m, \chi'_m \rangle \langle \psi_n, \psi'_n \rangle \tag{140}$$

If we assume discrete sets of eigenvalues k_{ym} and k_{zn}, then the corresponding modal functions $\chi_m(y)$ and $\psi_n(z)$ are not orthogonal with this inner product; however, the complex conjugates of the modes form a reciprocal basis. Inner products of the conjugate modes and the modes are then proportional to Kronecker delta functions:

$$\langle \chi^*_m(y), \chi_{m'}(y) \rangle = \overline{\chi^2_m} \delta_{mm'} \tag{141}$$

$$\langle \psi^*_n(z), \psi_{n'}(z) \rangle = \overline{\psi^2_n} \delta_{nn'} \tag{142}$$

$$\langle \phi^*_{mn}(y,z), \phi_{m'n'}(y,z) \rangle = \overline{\chi^2_m} \, \overline{\psi^2_n} \delta_{mm'} \delta_{nn'} \tag{143}$$

where the overbar symbol means the average over the spatial dimensions of the function.

C.2 Point Source in the Interior

The three-dimensional wave equation with a point source of volumetric strength S is

$$\nabla^2 \hat{p}_s + k^2 \hat{p}_s = \omega \bar{\rho} S \delta(x - x_0) \delta(y - y_0) \delta(z - z_0) \tag{144}$$

The pressure $\hat{p}_s$ can be expressed in a modal series, as in equation (11) in terms of the basis functions $\phi_{mn}(y,z)$, which satisfy the wall boundary conditions:

$$\hat{p}_s(x,y,z) = \bar{\rho} \bar{c}^2 \sum_{m,n=0}^{\infty} \mathcal{G}_{mn} \phi_{mn}(y,z) e^{ik_{xmn}|x - x_0|} \tag{145}$$

The combination of equations (144) and (145) gives

$$\bar{\rho}\bar{c}^2 \sum_{m,n=0}^{\infty} \mathcal{G}_{mn}\phi_{mn}(y,z)\left(\frac{\partial^2}{\partial x^2} + k_{xmn}^2\right) e^{\imath k_{xmn}|x-x_0|} = \omega\bar{\rho}S\delta(x-x_0)\delta(y-y_0)\delta(z-z_0), \quad x \neq x_0 \tag{146}$$

If we utilize the reciprocal basis function to form inner products and integrate over the $\delta(x-x_0)$ function, we obtain an equation for the coefficients $\mathcal{G}_{mn}$. This leads to the condition

$$\mathcal{G}_{mn} = -\frac{\imath}{2}\mathcal{Z}_{mn}\left(\frac{S}{HW\bar{c}}\right)\left[\frac{\chi_m(y_0)}{\overline{\chi_m^2}}\right]\left[\frac{\psi_n(z_0)}{\overline{\psi_n^2}}\right] \tag{147}$$

C.3 Point Source in the Left Boundary

Let the left boundary be a hard wall with a point source of strength S_w at a point (y_0, z_0). Then, the admittance in the general boundary equation (2) is zero, and

$$\hat{u}_s = S_w\delta(y-y_0)\delta(z-z_0) \tag{148}$$

The velocity is expanded in a modal series as

$$\hat{u}_s(x,y,z) = \bar{c}\sum_{m,n=0}^{\infty} \mathcal{U}_{mn}^{s+}\phi_{mn}(y,z)e^{\imath k_{xmn}x} \tag{149}$$

By evaluating this expression at $x = 0$,we obtain the coefficients of the expansion

$$\mathcal{U}_{mn}^{s+} = \left(\frac{S_w}{HW\bar{c}}\right)\left[\frac{\chi_m(y_0)}{\overline{\chi_m^2}}\right]\left[\frac{\psi_n(z_0)}{\overline{\psi_n^2}}\right] \tag{150}$$

The pressure coefficients are given by the modal impedances

$$\mathcal{P}_{mn}^{s+} = \mathcal{Z}_{mn}\left(\frac{S_w}{HW\bar{c}}\right)\left[\frac{\chi_m(y_0)}{\overline{\chi_m^2}}\right]\left[\frac{\psi_n(z_0)}{\overline{\psi_n^2}}\right] \tag{151}$$

These coefficients differ from those for a source in the interior only by the factor $-\imath/2$. Note that a volumetric source in the wall is twice as effective as a volumetric source in the interior.

C.4 Transmitted Power and Intensities for a Point Source

The acoustic intensity at a point (x, y, z) is given by

$$I_x(x,y,z) = 2\Re[\hat{p}\hat{u}^*] \tag{152}$$

where the superscript asterisk denotes the complex conjugate and $\Re$ is the real part. The power transmitted in the axial direction is given by

$$W_x(x) = \int_{-H/2}^{H/2}\int_{-W/2}^{W/2} I(x,y,z)dydz = 2HW\,\langle\hat{u},\hat{p}\rangle \tag{153}$$

The inner product $\langle \hat{u}, \hat{p} \rangle$ is

$$\langle \hat{u}, \hat{p} \rangle = \bar{\rho}\bar{c}^3 \sum_{m,n=0}^{\infty} \sum_{m',n'=0}^{\infty} \mathcal{P}_{mn} \mathcal{U}^*_{m'n'} e^{\imath(k_{xmn} - k^*_{xm'n'})|x-x_0|} \langle \chi_{m'}, \chi_m \rangle \langle \psi_{n'}, \psi_n \rangle \tag{154}$$

In the case of hard walls, the modes are orthogonal, and the inner products of modes become Kronecker delta functions. The power formula then simplifies to a double sum:

$$\langle \hat{u}, \hat{p} \rangle = \bar{\rho}\bar{c}^3 \sum_{m,n=0}^{\infty} \mathcal{P}_{mn} \mathcal{U}^*_{mn} e^{-2\Im(k_{xmn})|x-x_0|} \tag{155}$$